Synthesis of High Entropy Alloy for Surface Modification by Friction Stir Process: Recent Advances and Future Directions

S. Ragunath[1] · N. Radhika[1] · S. Aravind Krishna[1] · N. Jeyaprakash[2]

Abstract

High Entropy Alloys (HEAs) certainly stand out lately because of their uncommon mechanical properties and possible applications in different fields. Friction Stir Processing (FSP), a solid-state processing technique, has been displayed to upgrade the microstructure and mechanical properties of HEAs. This review article sums up the present status of-the-specialty of FSP applied to HEAs. The microstructural development and the processing parameters of FSP-treated HEAs are discussed and reviewed. The impacts of FSP on the grain structure, texture, and phase distribution of HEAs are featured. Moreover, the impact of FSP on the mechanical properties, like ultimate tensile strength, yield strength, microhardness, tribological behaviour, and corrosion properties of HEAs and HEA-reinforced metals is explored. Finally, possible applications and the difficulties and future headings of FSP applied to HEAs are examined. The review aims to give an outline of the recent progressions in the FSP of HEAs and inspire further research in this field.

Keywords High entropy alloys · Friction stir processing · Grain refinement · Microstructural influence · Mechanical properties

1 Introduction

In materials science, the traditional materials could not meet industrial requirement in the past decade. The material properties are altered by adding a few amounts of other elements to primary alloys such as the softening property of silver could be improved by the addition of copper; carbon and chromium are added with steel to make an enhanced strength and corrosion resistance [1]. The various percentile combination of traditional alloys including aluminium, steel, magnesium, copper, and superalloys are used in many applications for a long term to meet different requirements. However, these alloys have certain limitations such as the microstructure and material properties being changed by the addition of the elements [2, 3]. In the current scenario, the progression of material characteristics is essential to meet engineering and medical applications. Hence, composite materials such as Metal Matrix Composite (MMC), polymer matrix composite, and ceramic matrix composite are used from the last decade. Composite materials are most widely used to improve mechanical properties, wear, corrosion behaviour, and specific strength for several industrial applications [4, 5]. In the past decade, to improve the properties of Al and alloys, the reinforcement particles are added and termed as Aluminum Matrix Composites (AMCs), moreover metallic glasses, ceramic particles, and nano-tubes are typically utilized as reinforcements [6–8]. The reinforced ceramic particles with Al—composites struggle to meet current industrial demand due to their poor interfacial bonding and wettability between matrix and reinforcements, and the physical and chemical nature of added materials [9–11]. SiC, TiC, B_4C, Al_2O_3, TiO_2, and MoS_2 are used as reinforcement materials in MMC to enhance mechanical and tribological properties [12–14]. The defects such as porosity, particle fragmentation, cracks, insufficient wettability, and reinforcement agglomerations are observed and lead to the declined properties of the composites limiting its application [15, 16]. A novel material is required to overcome these drawbacks and meet the present challenges in industrial application.

✉ N. Radhika
  n_radhika1@cb.amrita.edu

1   Department of Mechanical Engineering, Amrita School of Engineering, Amrita Vishwa Vidyapeetham, Coimbatore, India

2   School of Mechanical and Electrical Engineering, China University of Mining and Technology, Xuzhou 221116, China

High Entropy Alloy (HEA) is introduced in the field of materials science in the twenty-first century to meet the current demand in the engineering and medical sectors [17]. HEA has a single-state solid solution of multi-component elements with a unique microstructure. The lower Gibbs free energy, higher entropy, and less enthalpy leads to impede the segregation of elements and make a stable solid solution. Hence, the inter-metallic components are prevented by the stable solid solution [15, 18, 19]. These materials have higher thermo-mechanical stability, superior tensile properties such as ductility, and Ultimate Tensile Strength (UTS) at ambient and elevated temperatures, better wear and corrosion behaviour. Moreover, the HEA can be applicable to both structural and functional requirements in industries [20–22]. The available categories of HEAs are illustrated in Fig. 1. The elements Al, Be, Li, Mg, and Ti have a density below 6 g/cm^3 and are termed as lightweight HEAs. These alloys are designed for wear and oxidation-resistant components alongside high-temperature applications [23, 24]. The high-temperature materials such as Cr, Hf, Mo, Nb, Ta, V, W, and Zr are categorized as refractory HEAs and applicable in the field of defense, nuclear, and aerospace industries [25, 26]. The elements—Ru, Ir, Rh, Pd, Pt, and Os are precious and are categorized as a precious group of HEAs [27, 28]. In the multistep reactions, the precious group of HEAs acts as the ideal catalysts. The elements Lu, Dy, Tm, Gd, Y, and Tb are categorized as lanthanide HEAs [29]. The minimum four elements combination of Fe, Al, Cr, Cu, Co, Mn, V, and Ni are referred to as 3D transition metal leads to more stability at elevated temperatures [30, 31]. The B, C, and N elements

are categorized under the group of interstitial HEAs. These HEAs are used in the field of magnetocaloric applications due to their thermodynamic stability, magnetic ground-state structure, and magnetocrystalline anisotropy energy [32]. The addition of Al, Sn, and Zn to equiatomic alloys (CuMnNi) are categorized as brasses and bronzes HEAs to improve hardness and strength [33]. The four major effects such as the high-entropy effect, cocktail effect, lattice distortion, and sluggish diffusion influence the microstructure and phase of HEAs during the synthesis. The entropy of mixing, atomic size difference, and enthalpy of mixing are predominant factors for the formation of the inter-metallic phase in the multi-component elements during the synthesis of HEA. These features could be governed by the high-entropy effect. The cocktail effect is used to attain exceptional properties in HEA by mixing the different elements in various percentiles. In a crystal lattice, the various atoms are arranged randomly by lattice distortion. The strengthening of HEA could be obtained by grain structure and fine precipitates due to the sluggish effect [20, 34].

Noteworthy, the HEA exhibits more refined and improved properties than traditional alloys since HEAs are design-based alloys [35]. Further enlargement in the properties of HEA is required for modern material industries to meet the requirements in engineering and medical applications. Hence, the HEA particles are processed by novel techniques for additional enhancement of their properties [36]. The researches bring in a new single-step process namely Friction Stir Process (FSP) which is delivered from friction stir welding technology with a similar working principle [37]. FSP is used to enhance the material properties through microstructural modification and grain refinement due to the severe plastic deformation in the processed zone [38–40]. The FSP is employed as an alternative technique to MMC to overcome the challenges by localized microstructural modification. The process is conducted below the melting temperature of the base metal. Hence, FSP could not affect the physical nature of the base metallic structure [41]. The main characteristics of FSP are grain size reduction that is evenly dispersed on the base metal through severe plastic deformation in single-step processing. The process parameters influence the material properties by refined grains in the processed zone. Moreover, being eco-friendly and the nature of less energy consumption, FSP gains more attention [42, 43]. The casting defects are eliminated by refined grains and inter-metallic phases are also deformed by severe plastic deformation, which improves mechanical properties [44, 45]. Considerable research work is successfully processed by FSP on Al, Mg, Cu, steel, and its composition for different applications. The research conducted on HEA and FSP over the years is shown in Fig. 2.

The one-step FSPed as-cast metal with HEA exhibits excellent interfacial bonding, dynamic recrystallization,
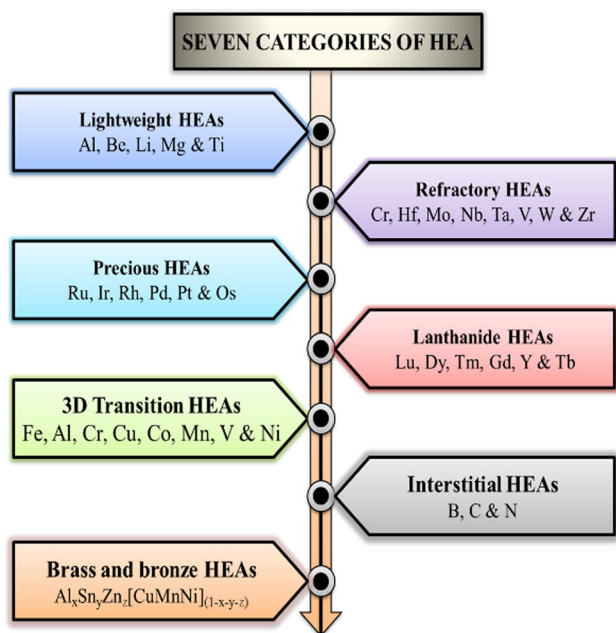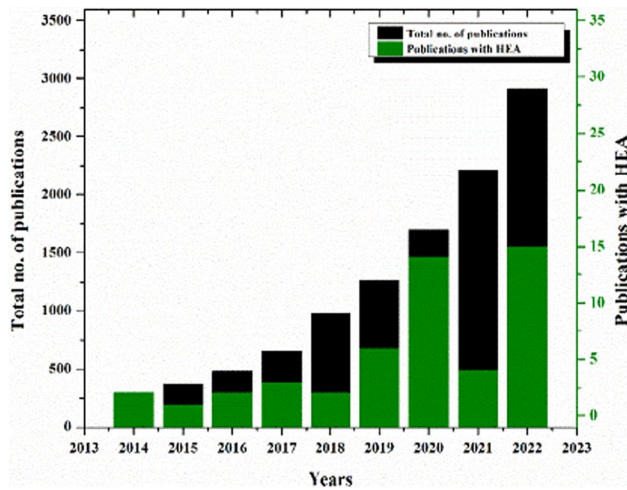

Fig. 1 Classification of HEAs

Fig. 2 Number of articles published on the topic HEA and FSP (source: Scopus)


Fig. 3 Induced mechanisms during FSP

fine grains, grain refinement, homogeneous distribution of reinforcements, and thermo-mechanical stability. These features are responsible for improved hardness, toughness, tensile properties, fatigue resistance, tribological and corrosion behaviour at room and elevated temperatures [46–48]. The ultra-refined grain structure, effective mixing of the HEA particles with base metal, and evenly dispersed refined grains by pinning effect implies the improved properties of base metal through FSP. These factors are validated by Hall–Petch relations, and the rule of mixtures [49, 50]. Moreover, the Orowan strengthening mechanism, twining mechanism, quench hardening effect, Particle Stimulated Nucleation (PSN) effect, and barrier effect of the HEA particles are also responsible factors for hosting FSPed samples to industrial requirements [8, 51, 52]. Some of the induced mechanisms during FSP are shown in Fig. 3. In the concerned applications, FSP is a possible technique to modify the base metal with a required volume of reinforcements to enhance the mechanical properties by grain refinement and plastic deformation [53]. So far, the various HEA particles AlCoCrFeNi, CoCrFeCuTi, and CrMnFeCoNi with different atomic percentiles are reinforced with as-cast metals (Al, Cu, Mg, and steel) and their composites through FSP [54–56]. A significant grain reduction, phase formation, and microstructural modification in the Stir Zone (SZ) lead to the improvement in mechanical properties, fatigue behaviour, wear, and corrosion resistance [57]. Figure 4 illustrates the overall methodology of the FSP process from the HEA synthesis to meet the end application.

The HEA particles reinforced with as-cast metals through FSP and their microstructure characteristics, mechanical properties and their mechanisms have been reviewed. In this work, comprehensive details of HEA, synthesis of HEA, effect of machining and tooling process parameters,
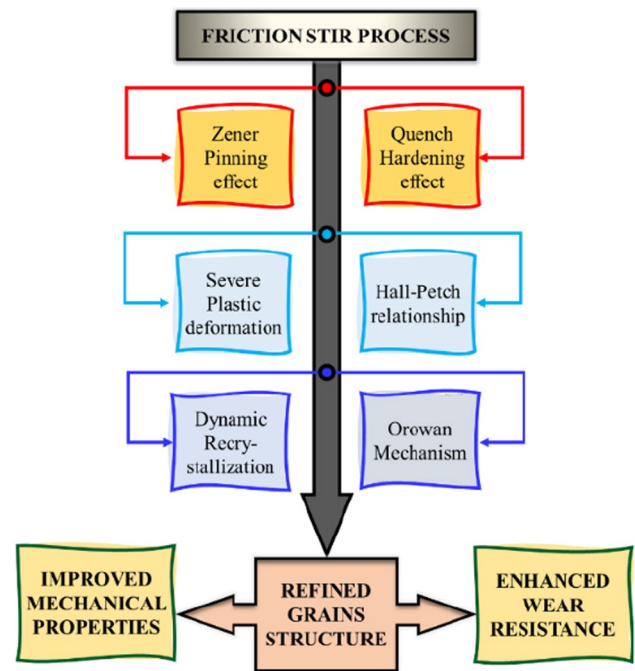
microstructural modification, the impact of phase structure in mechanical properties, wear and corrosion resistance of HEA/as-cast metal treated by FSP, future trends, and the applications are reviewed. In addition, the research gaps on HEA/as-cast metal with FSP, various issues on fabrication,
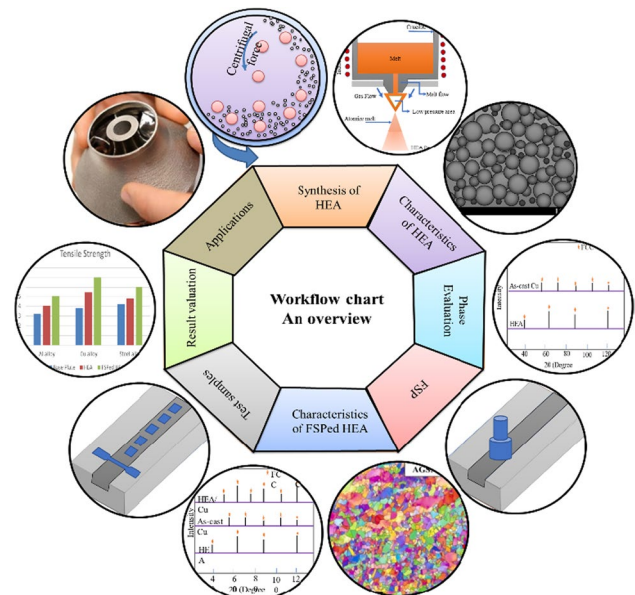
Fig. 4 Workflow chart of FSPed HEA—an overview on the HEA synthesis to end application

deformation mechanism, defect-free components, and future work to meet attention are provided.

2 High Entropy Alloy

The HEA consists of five or more multi-functional elements with equal or unequal percentiles. The principal elements used in HEA are made up of FCC structure (Al, Ni, Cu), BCC structure (Fe, V, Cr, Nb, Mo, Ta, W), and HCP structure (Co, Ti, Zr) [22]. The primary elements are used in the fraction of 5%–35%, and secondary elements are used below 5% for the fabrication of HEAs [58]. The stability of the HEA structure could be identified by Valence Electron Configuration (VEC). The high value of VEC (above 8) is beneficial to the formation of the FCC phase for higher ductility of HEAs. The low value of VEC (below 6.87) is conducive to the development of the BCC phase for improved strength of HEAs. The intermediate value of VEC (6.87 to 8) represents the combined FCC and BCC phase structure [59–61].

2.1 Synthesis of HEA for FSP

The synthesis of HEA is a crucial process to obtain a single-state solid solution and unique phase that leads to enhanced mechanical properties, wear resistance, and corrosion behaviour for various applications [62, 63]. The development of HEA is achieved by three major categories such as solid-state synthesis, liquid-state synthesis, and gas-state synthesis [20, 64]. The synthesis methods play significant role in their microstructure, grain size, phase formation, and stability. The powder form of HEA is used as reinforcement on the base metal through FSP. Mostly, mechanical alloying under the categories of solid-state synthesis is used to fabricate HEA powders that employed in FSP to enhance the strengthening properties of base metal [56, 65]. However, gas-atomized HEA powders are also effectively used for surface modifications under FSP [11, 66]. The planetary ball milling is a popular method to synthesize HEAs. Moreover, shaker rod mills, grinding vials, and SPEX mills are also used for

the fabrication of HEAs in mechanical alloying [67]. The dry and wet milling is also a factor to influences the fabrication of HEA powder in mechanical alloying. In wet milling, methanol, ethanol, stearic acid, dodecane, and n-heptane are used frequently as a milling medium. [18, 68, 69]. 45 h of dry milling and 4 h of wet milling by ethanol are employed to produce the $Al_{0.8}CoCrFeNiTi_{0.2}$ HEA particles [70]. A nano-crystal structure is obtained on $Al_2NbTi_3V_2Zr$ HEA synthesis through high energy ball milling with 350 rpm milling speed [71]. The milling parameters such as duration of milling, surrounding medium, types of milling, and their speed are responsible for obtaining a single-phase solid solution of HEA [72].

$Fe_{23}Cr_{21}Ni_{18}Ti_{20}Mn_{18}$ HEA powders are synthesized by planetary ball milling at 300 rpm for 15 h in a toluene atmosphere to avoid oxidation. The solid solution attains after 15 h milling due to the bonding of principal elements, atomic size difference, high entropy effects, and uniform distribution of constituent elements. 5–7 μm refined HEA particles are obtained due to the severe plastic deformation and work hardening of elements which improves surface energy for electrochemical applications. The addition of milling duration leads to minimizing crystallite size and increases the lattice strain and its parameters [73]. The mechanical alloying $Zr_xFeNiSi_{0.4}B_{0.6}$ HEA particles exhibit an amorphous structure. The addition of Zr (x = 1, 1.5, 2.5) leads to a faster growth of the amorphous phase and an increased ability of amorphous formation. In the agglomeration state, the near-spherical particles are separated by small lamellae particles at 180 hrs milling and the particle size reduced with increment of the Zr ratio shown in Scanning Electron Microscope (SEM) images (Fig. 5). The FCC phase structure and some amorphous structures are obtained on $Zr_xFeNiSi_{0.4}B_{0.6}$ (x = 1,1.5,2.5) with more thermal stability [74].

The CrMnFeNiCu HEA particles fabricated by high energy planetary ball milling exhibit a single solid solution with a few radii differences of quinary elements used. The 40 h of ball-milling exhibits a fine grain size and high lattice strain of BCC and FCC structures. The ductile elements like Fe, Ni, and Cu are used to improve formability
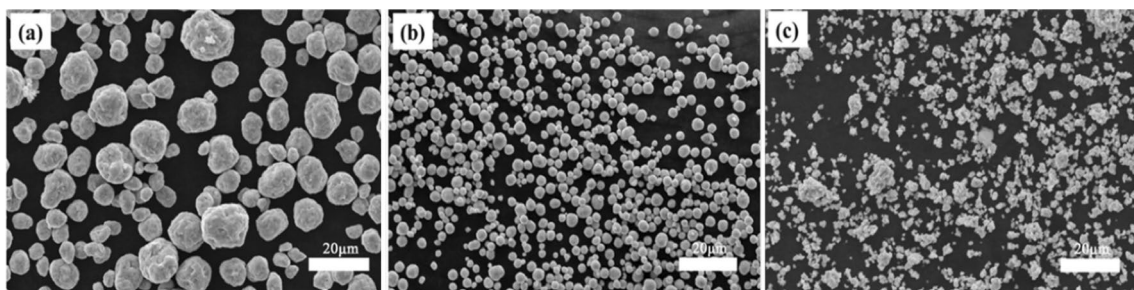

Fig. 5 SEM images of $Zr_xFeNiSi_{0.4}B_{0.6}$ HEA after 180 h milling. **a** at x = 0.5, **b** at x = 1.5, **c** at x = 2.5 [74]

for structural applications, and brittle elements like Cr and Mg are used for higher strength and hardness. The formation of inter-metallic compounds is hindered by lower Gibbs energy and high entropy ascribed to the attainment of a stable single solid solution during synthesis. In addition, higher entropy and less enthalpy are employed to fabricate a single solid solution of HEA. These features lead to strengthening and avoid phase transition during synthesis even though the difference in coefficient of thermal expansion exists in HEAs [75]. The synthesis of $Fe_{1.8}Co_{1.8}Ni_{1.8}Cr_{1.8}Mn_{1.8}Al_{1.0}$ HEA particles by high energy planetary ball milling leads to reduced grain size by the addition of NaCl powder. The synthesized milling time is optimized by the statistical Fisher-Pearson coefficient of skewness and kurtosis. The alloy formation starts with 20 h of milling and the peaks of principal elements vanish by addition of milling time as shown in the X-ray Diffraction (XRD) pattern in Fig. 6a [76]. The ball-milled AlFeTiCrZnCu HEA powder exhibits a single-phase solid solution by maximized configurational entropy. A high energy planetary ball milling speed of 300 rpm for 20 h milling with WC vial and toluene is used as a Process Controlling Agent (PCA) to attain 10 nm particle size along BCC structure. The intermetallic peaks are varnished and single-phase solid solution formation started by 10 h milling. The complete solid solution for hexanary elements appeared by 20 h milling as shown in the XRD pattern (Fig. 6b). The increasing number of constituent elements requires a long duration due to the slower diffusivities

[77]. $Ni_{1.5}CoCuFeCr_{0.5-x}V_x$ (x = 0.25,0.5) HEA powders are synthesized by ball milling with 300 rpm for 70 h. The powders are formed after 66 h of dry milling under Ar atmosphere and 4 h of wet milling in ethanol. A major phase of FCC and a few BCC phases appeared with a crystalline size of 10 nm as shown in the XRD pattern (Fig. 6c) [78]. The equiatomic CoCrFeNiMnAl HEA particles are fabricated by the ball milling process. A strong BCC and weak FCC phase structure appeared after 60 h milling of constituent elements (Fig. 6d). The nanocrystalline grains of 20 nm size of better consistency obtained by maximum milling [79].

A ball milling is employed to fabricate $CoNiFeAl_{0.4}Ti_{0.6}Cr_{0.5}$ HEA particles with the irregular shape of a mean grain size of 7 nm. The peaks are minimized continuously over the increment of milling time as shown in the XRD pattern (Fig. 6e). A major BCC and minor FCC phase structures appeared after 60 h of milling. [80]. Ball-milled CoCrFeNiMn HEA particles exhibit FCC and BCC phase structures with a 10 nm size by 250 rpm for 60 h under the Ar atmosphere. Cold welding and metal oxidation are prevented by PCA of N-heptane. Initially, diffraction peaks of constituent elements appeared and decreased with the increment of milling time as shown in the XRD pattern (Fig. 6f). A high lattice strain, refined crystal size, and reduced crystallinity contribute to the formation of HEA particles effectively [81]. The major FCC and minor BCC phase structures are obtained in the synthesis of FeCrCoNiCu HEA particles for 50 h by planetary ball milling. Dislocation density and
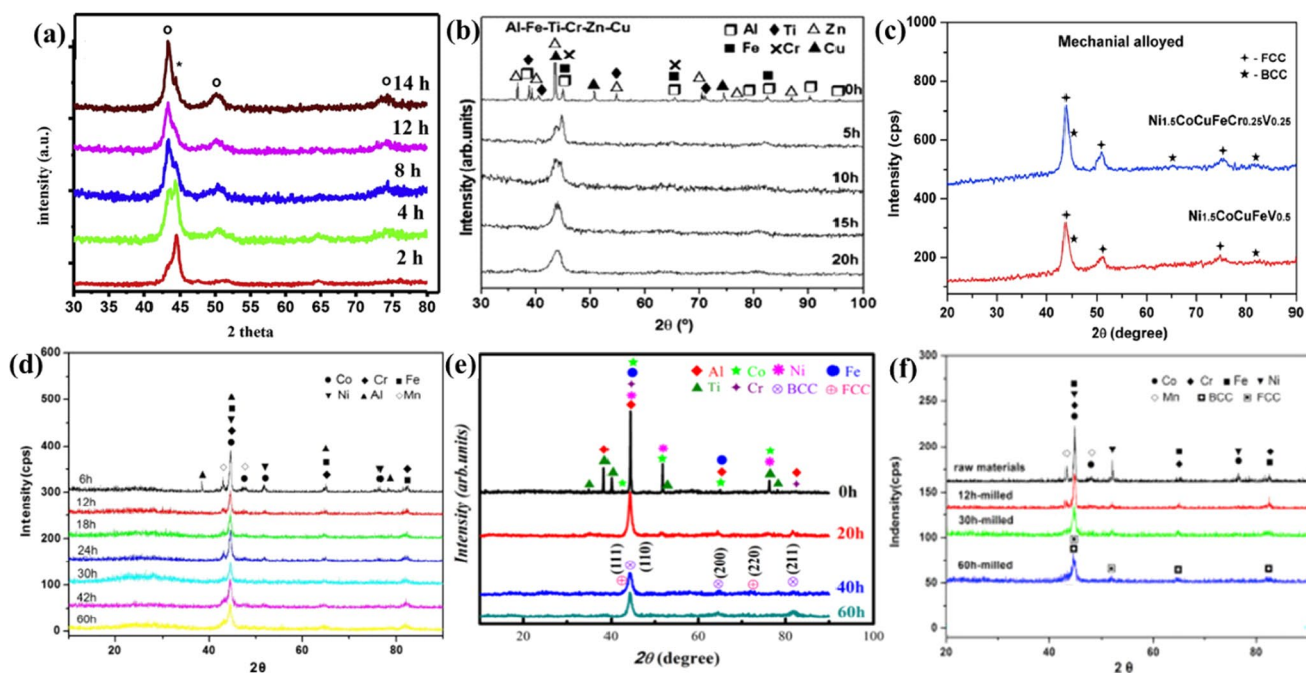
Fig. 6 XRD patterns. **a** $Fe_{1.8}Co_{1.8}Ni_{1.8}Cr_{1.8}Mn_{1.8}Al_{1.0}$ HEA powder for 14 h milling [76], **b** AlFeTiCrZnCu HEA powder for 20 h milling [77], **c** $Ni_{1.5}CoCuFeCr_{0.5-x}V_x$ HEA powder for 70 h milling [78], **d** CoCrFeNiMnAl HEA powder for 60 h milling [79], **e** $CoNiFeAl_{0.4}Ti_{0.6}Cr_{0.5}$ HEA powder for 60 h milling [80], **f** CoCrFeNiMn HEA powder for 60 h milling [81]

strain rate are increased by the continuous deformation of HEA powders. Cold welding occurs during the formation of HEA due to the deformation of powders by ductile and soft nature which results in agglomeration of particles in the size of 3–36 μm. The continuous deformation of powders by increment of milling, and decreasing cold welding leads to reducing particle size in the range of 5–32 μm. The homogenous distribution of HEA powders with a reduced grain size of 4–21 μm obtained by the 50 h milling. Figure 7 shows the distribution of particles by 10, 30, and 50 h milling time [82].

Gas atomization is a common method used to produce metal powders with a relatively uniform size distribution of HEA particles. This technique prevents thermal distortion and is the most frequently used process for commercial scale. The resulting powder particles can have relatively consistent sizes. The use of gas atomization for producing metal powders can be economically viable for certain applications, especially when high-quality, uniform-sized powders are required [83]. High thermo-mechanical stability with spherical shape HEA powder exhibits a high purity of single solid solution in composition and morphology examination [84]. The gas atomization is accomplished in a short time with less tendency of particle contamination [85, 86]. The $Al_{0.5}CoCrCuFeNiSi_x$ (x = 1, 1.2, 2) HEA particles are synthesized by the gas atomization method. A fast-cooling rate with the addition of Si reduces segregation and improves the solid solution strengthening effect without changing the

crystalline structure. The spherical-shaped particles with smooth surfaces are obtained in the mean size of 27 μm (Fig. 8a). Few impurities are observed on HEA powders due to the turbulent flow and collisions in the atomization chamber. The FCC and BCC phase structures appeared with sharp diffraction peaks by the XRD pattern (Fig. 8b). The sharp peaks with reduced width confirm the higher crystallinity of powders. The high solidification rate leads to a single solid solution in HEA powders [84]. AlCrCoNiCu HEA particles are fabricated by gas atomization with a spherical shape of FCC phase structure. The synthesized powders offer good flow-ability, homogenous composition, and stable performance with a particle size of 10–50 μm. The dual phases of FCC and BCC structures appear by the addition of Fe and Mn. The refined particle of HEA powders attributes even shape and reduces surface roughness [87]. $Al_{0.5}CoCrFeNi_2$ HEA powders are synthesized by the gas atomization process. The spherical-shaped particles appear with a size of 60–90 μm (Fig. 8c). The constituent elements of HEA powders are evenly distributed with a single-phase FCC structure. The rapid cooling process of gas atomization prevents phase segregation effectively [88].

The gas atomization is used to fabricate a spherical shape of AlCoCrFeNi HEA particles with a single-phase B_2 structure. At 900–1000 °C, the B_2 phase of the HEA particles is transferred to triple phase A_2, B_2, and FCC structures due to oxidation is shown in the XRD pattern (Fig. 8d). The obtained triple phases lead to increased boundary density
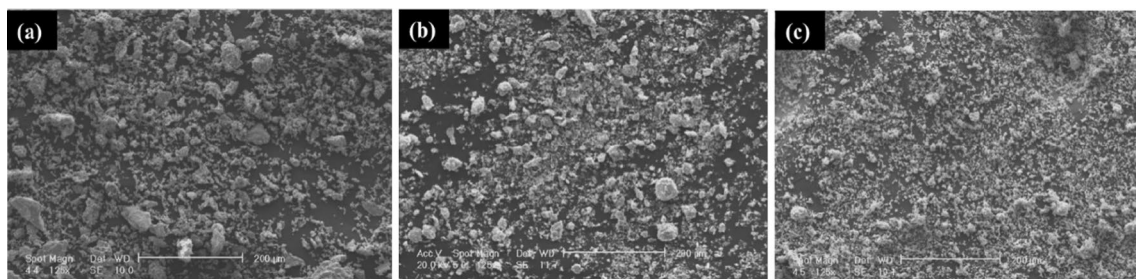
Fig. 7 SEM images. **a** 10 h, **b** 30 h, **c** 50 h ball milled FeCrCoNiCu HEA powders [82]
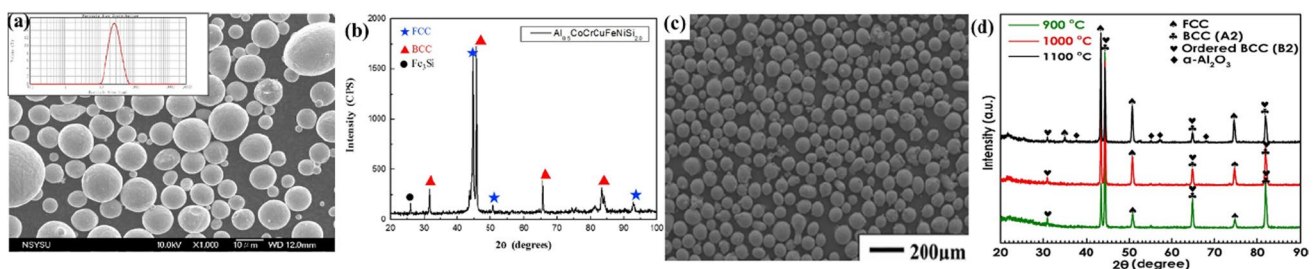
Fig. 8 **a** SEM image of $Al_{0.5}CoCrCuFeNiSi_x$ HEA powder [84], **b** XRD pattern of $Al_{0.5}CoCrCuFeNiSi_x$ HEA powder [84], **c** SEM image of $Al_{0.5}CoCrFeNi_2$ HEA powder [88], **d** XRD pattern of AlCoCrFeNi HEA powder [89]

and the formation of Al_2O_3 scale. Due to thermodynamic equilibrium, the σ phase is obtained instead of the A_2 phase after 48 h of oxidation. Finally, single-phase FCC structure started appearing after 48 h due to diffusion of Al. The failure could be delayed due to less driving force which is obtained from the residual stress of Al_2O_3. The HEA powders are undergone polishing and etching for phase constitutions. The wide distribution of equiaxed grains appeared on the gas-atomized HEA powders. The high magnification of BSE images shows no color contrast which confirms the single-phase structure as shown in Fig. 9 [89]. Spherical-shaped AlCrCuFeNi HEA particles are fabricated by gas atomization. 4–6 μm average size of particles is obtained with a single-phase BCC structure and etched in HNO_3 solution, which exhibits evenly dispersed nano-sized pores [90]. Table 1 presents the various synthesis methods to fabricate HEA by different elemental compositions for FSP. The developed phase structure with grain size is also mentioned for concern HEA particles.

3 Friction Stir Processing

The FSP technique is widely used to achieve fine grain structure by severe plastic deformation [102, 103]. FSP is a solid-state technique to refine the grains of metallic materials through single-step short processing than conventional methods [41, 42]. FSP is responsible for producing refined grains in the processed zone of as-cast metal with or without reinforcement materials and generates a homogeneous microstructure, thereby increasing the thermo-mechanical stability, tensile properties, ductility, microhardness, wear, and corrosion resistance for concerned engineering applications [11, 104]. There are several methods available to increase the wear resistance of the samples such as surface modification, coating techniques, thin film deposition, altering the metallurgical bonding, and texturing of deposits [105, 106]. Among the above methods, FSP, one of the surface modification techniques, plays a vital role in enhancing the mechanical properties, wear, and corrosion resistance [107, 108]. The sequence of the FSP is illustrated in Fig. 10.

FSPed samples exhibit refined grains and are evenly dispersed over the base metal through single-pass or multi-pass processing techniques. The enhanced properties of FSPed samples are attributed by refined grains due to the machining parameters and tooling parameters employed. FSP is a multifunctional process and there are no further accompanying processes required. The refined grain structure is evenly dispersed on base metal with High Angle Grain Boundaries (HAGBs) and dislocation density is obtained on the FSPed samples to enhance mechanical and wear properties. FSP involves grain size reduction of base metals and extends the development of surface composites by the addition of reinforcement that increases mechanical properties to serve the industrial applications [109–111].

The machining and tooling parameters are the process parameters which contributes to enhance the properties (Fig. 11). The control of processing parameters such as rotational speed, traverse speed, tilt angle, number of passes used, axial force on the tool, tool pin profiles, plunge depth, and tool materials improve the mechanical, wear and corrosion through dynamic recrystallization and severe plastic deformation by induced frictional heating [112]. The heat developed by FSP due to friction between the tool and work materials leads to an ultrarefined grain structure in the processed zone. Hence, sufficient temperature and strain rate are maintained during FSP [38]. The better-refined structure attained by FSPed samples through higher traverse speed and lower rotational speed leads to an improved strengthening mechanism. Moreover, an uneven distribution of reinforcement particles appeared on the base metal due to the excessive addition of traverse speed during FSP. The combination of maximum rotational speed with minimum traverse speed and minimum tool travel per revolution exhibits a coarse grain structure and implies a reduction of the hardness of FSPed samples [104]. Hence, the combination of traverse and rotational speed is selected depending on the work and tool materials and surrounding environments.

The casting defects such as porosity and micro-cracks are to be eliminated or minimized by FSP through grain reduction, frictional heating, plastic deformation, and the addition of reinforcement materials. The higher tool rotational speed, and low traverse speed lead to maximum frictional heat and high plastic deformation during FSP and eliminate the defects. The grain refinement is obtained by frictional heat that increases the

Fig. 9 SEM images. **a** Equalized grains, **b** Grain boundaries with high magnifications [89]
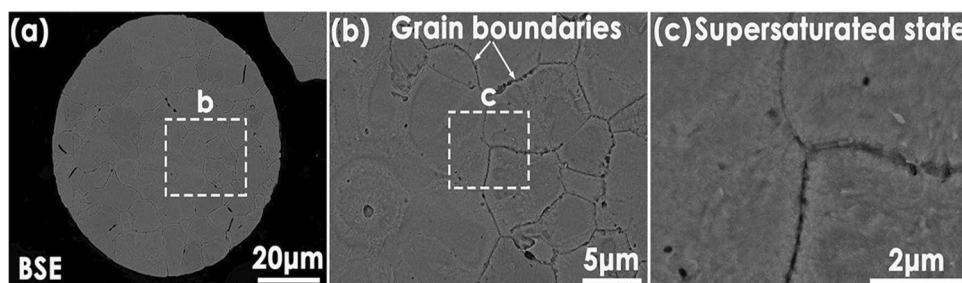
Table 1 The synthesis of HEA particles for FSP and obtained phase structure

Synthesis methods	Composition of HEA particles	Phase structure	Grain size	Ref
Mechanical alloying	$CoCrFeNiMo_{0.4}$	FCC	40–70 μm	[3]
	CoCrFeCuTi	BCC	17 μm	[56]
	AlSiBeTiV	FCC	15 μm	[65]
	$Al_{0.8}CoCrFeNiTi_{0.2}$	BCC + FCC	–	[70]
	$Al_2NbTi_3V_2Zr$	BCC	5 μm	[71]
	$Fe_{23}Cr_{21}Ni_{18}Ti_{20}Mn_{18}$	–	5–7 μm	[73]
	$Zr_xFeNiSi_{0.4}B_{0.6}$	FCC	1–3 μm	[74]
	CrMnFeNiCu	FCC + BCC	15.69–44.67 nm	[75]
	FeCoNiCrMn	FCC	0.5–5 μm	[76]
	AlFeTiCrZnCu	BCC	10 nm	[77]
	$Ni_{1.5}CoCuFeCr_{0.5-x}V_x$	FCC + BCC	10 nm	[78]
	CoCrFeNiMnAl	BCC + FCC	20 nm	[79]
	$CoNiFeAl_{0.4}Ti_{0.6}Cr_{0.5}$	BCC + FCC	7 nm	[80]
	CoCrFeNiMn	FCC + BCC	10 nm	[81]
	FeCrCoNiCu	FCC + BCC	4–21 μm	[82]
	AlCoCrFeNi	BCC + FCC	10 μm	[91]
	$CoCrFeNiMo_{0.85}$	BCC + FCC	15	[92]
	NbMoTaWVTi	BCC	10	[93]
	CoCrNiCuZn	BCC	3	[94]
	CuNiCoZnAlTi	BCC	9 nm	[95]
	$Al_{0.3}NbTa_{0.8}Ti_{1.5}V_{0.2}Zr$	BCC	15–20	[96]
	$Al_{0.2}Co_{1.5}CrFeNi_{1.5}Ti$	FCC	–	[97]
Gas atomization	$Al_{0.8}CoCrFeNi$	BCC	6.5 μm	[11]
	AlCoCrFeNi	BCC	10.5 μm	[40]
	AlCoCrFeNi	BCC	10.5 μm	[66]
	$AlCoCrCuFeNiSi_x$	FCC + BCC	27 μm	[84]
	AlCrCoNiCu	FCC + BCC	10–50 μm	[87]
	$Al_{0.5}CoCrFeNi_2$	FCC	60–90 μm	[88]
	AlCoCrFeNi	FCC + BCC + α–Al_2O_3	45–105 μm	[89]
	AlCrCuFeNi	BCC	4–6 μm	[90]
	AlCrCuFeNi	BCC	4–6 μm	[98]
	AlCoCrFeNi	BCC	20 μm	[99]
	AlCoCrFeNi	–	5–23 μm	[100]
	CoCrFeNi	FCC	24.7 μm	[101]

strengthening mechanism of FSPed samples [112, 113]. FSP is used effusively to improve the mechanical properties of samples by refining the grain structure and dynamic recrystallization [42, 114]. Moreover, further improvement of the FSPed samples can be achieved by the addition of Nitrogen alloy which leads to enhancing strength, toughness, and corrosion resistance [115, 116]. The formed weak interfacial layer between reinforcement and base metal could be minimized by the submerged FSP. In addition, the temperature rise and thermal cycle are reduced effectively with the help of cooling water added externally during FSP [66, 117, 118].

3.1 Influence of Machining Parameters on Microstructure and Mechanical Properties

3.1.1 Rotational Speed

The tool can be rotated either clockwise or counterclockwise direction along its axis by the rotational speed which is generated by the FSP machine [119]. The mechanical properties of Cr reinforced Nickel Aluminium Bronze (NAB) composites are optimized by Taguchi and Grey relational analysis. The UTS, yield strength, microhardness, and microstructural modifications are analyzed by varying rotational speed by
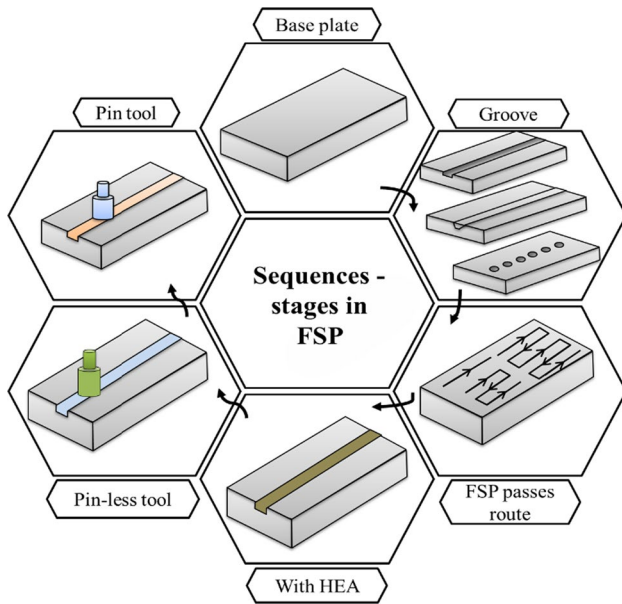
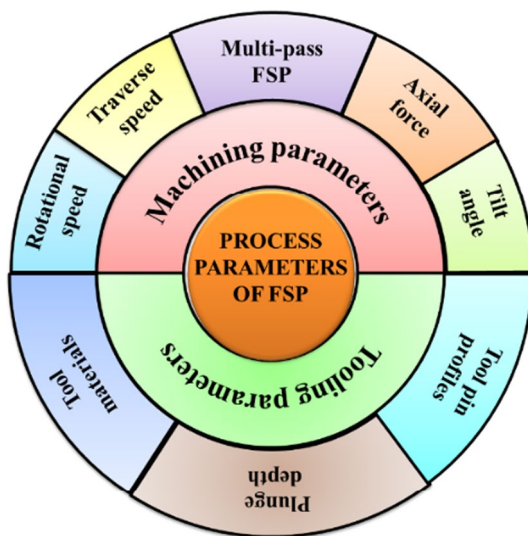**Fig. 10** Various stages involved in the FSP process


Fig. 11 Process parameters in FSP

710, 1000, and 1400 rpm at 28 mm/min traverse speed. The rotational speed of 1000 rpm exhibits enhanced results in UTS, yield strength, and microhardness by 13.6%, 33.7%, and 34.4%. The abrasive wear mechanism is obtained from adhesive and the wear rate is reduced by 27.3%. The fine and equalized grains are observed in the SZ through severe plastic deformation and recrystallization. A significant plastic deformation obtained by induced frictional heat leads to grain refinements [120]. However, the induced frictional heat is one of the factors to influence the grain refinements in addition to the rotational speed and traverse speed. The

higher heat generates more growth of grains leading to a coarse nature and lower heat generates porosity with cracks during FSP [104, 121]. FSP is conducted on A319 alloy to improve the tensile strength and microhardness by 50% and 20% over the base metal with 1200 rpm among the five different rotational speeds of 800, 1000, 1200, 1400, and 1600 rpm. The enhanced strength and microhardness are obtained by minimizing defects such as blow holes, cracks, and porosity through the generation of frictional heat by FSP. The material flow and intense plastic deformation are attributes through the stirring action of the tool that leads to fine grain structures. The optical macrograph and SEM micrograph show the effect of rotational speed in the processed zone (Fig. 12). The pinhole and micro-void defects are observed under the 800 and 1000 rpm rotational speeds. The defect-free surfaces with an elliptical and classical onion ring, basin-shape, and indiscernible shape are detected from 1200, 1400, and 1600 rpm rotational speed. A significant frictional heat is generated by the rubbing action of the tool pin with the workpiece. The defect-free surfaces are obtained in SZ with refined grain structure through the synergetic effect of frictional heat and deformation due to the stirring action of the tool with pressure by the tool shoulder [122].

FSP is employed to reinforce 0.25 to 0.42 μm size Si particles on A356 through varying rotational speeds of 300, 500, 700, and 900 rpm. The defect-free surfaces exhibit through the evenly distributed equalized grains by 900 rpm. A high rotational speed and stirring action of the tool attribute frictional heating that generates an even distribution of uniform grains in the SZ. The coarse grains and cluster form of Si particles are observed under the low rotational speed due to insufficient frictional heating [39]. The Si particles are reinforced with pure Al by FSP at varying rotational speeds of 500, 700, and 1000 rpm. It is observed that the even distribution of uniform grains is achieved by 1000 rpm rotational speed. The hardness and bending strength is improved by 1.23 and 1.14 times by refined grains, uniform dispersion, and sufficient friction heat. The severe plastic deformation and sufficient frictional heat attribute a reduction of porosity, dissolution of precipitates fragmentation of coarse dendrites, and second-phase particles that generate a fine uniform grain distribution, and defects-free surfaces. The induced frictional heating is one of the major governing mechanisms through extensive plastic deformation [123]. A 200 nm grain size is attained on the A5083 composite by reinforcing fullerene through FSP with different rotational speeds of 500, 1000, 1500, and 2000 rpm. The hardness of FSPed samples is improved by double the times of base metal due to the grain refinements by pinning effects, equalized grains, and even dispersion of fullerene by effective material flow over the A5083 composite. A significant material
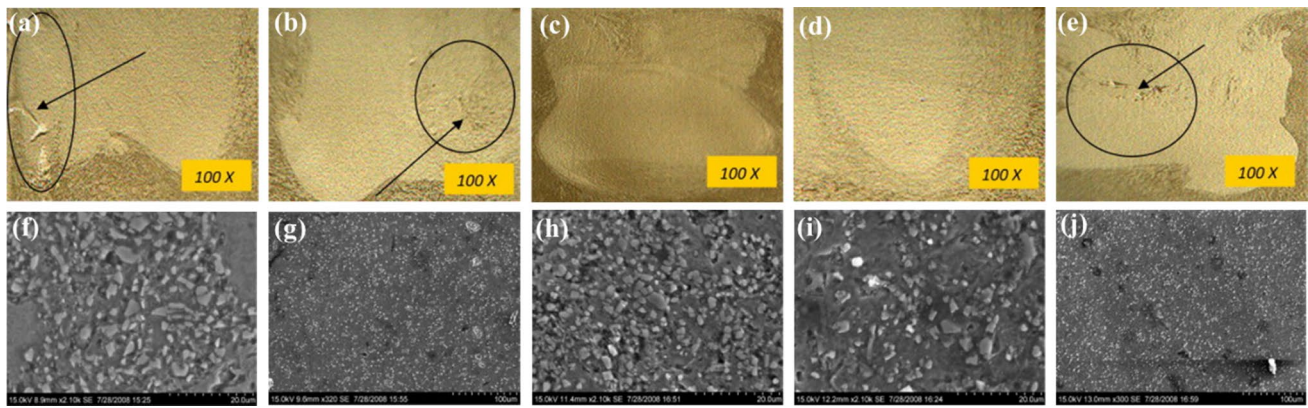
Fig. 12 Optical macrograph and SEM micrograph. **a, f** 800 rpm, **b, g** 1000 rpm, **c, h** 1200 rpm, **d, i** 1400 rpm, **e, j** 1600 rpm rotational speeds [122]
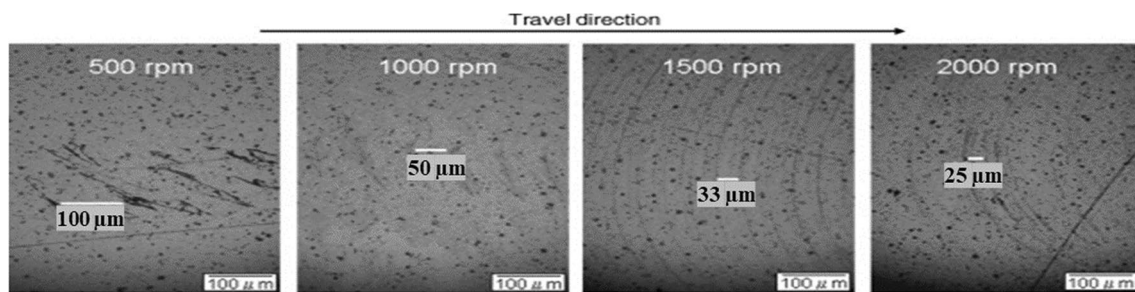
Fig. 13 Optical microscopy of lateral sections under various rotating speeds [124]

flow is observed by the increment of rotational speed due to the formation of the onion ring as shown in Fig. 13. A strong onion ring is observed by sufficient frictional heat which is generated on the frictional contact of the tool and workpiece [124]. A 5 wt% of TiC is reinforced on pure Al base material through FSP with varying rotational speeds of 640, 800, and 1000 rpm and traverse speed of 60, 120, and 150 mm/min. The hardness and UTS are improved by 26.3% and 18.9% due to the grain refinement by sufficient induced frictional heat. The higher ratio of rotational speed and traverse speed leads to softening and plasticizing the material, which generates efficient flow over the FSP tool to produce defect-free surfaces on the SZ. The significant heat is produced on a higher ratio by 1000 rpm rotational speed and 60 mm/min traverse speed [125]. The Al_2O_3 powders are reinforced on AZ31 by FSP at 800, 1000, and 1200 rpm of rotational speed and 45 mm/min traverse speed for surface applications. The efficient nanoparticle distribution is attained by the result of significant heat, refined grains, and simultaneously more shattering effect of rotation which is caused by increment of rotational speed. A significant heat and material flow is obtained on FSPed samples by higher rotational speed due to the minimized cluster size of alumina particles [126].

3.1.2 Transverse Speed

The direction of the FSP tool towards the workpiece is controlled by transverse speed. The effect of different transverse speeds of 28, 40, and 56 mm/min are evaluated on the Cr-reinforced NAB composite by FSP. The improved UTS, yield strength, and microhardness of 701 MPa, 335 MPa, and 385 HV are observed at the minimum transverse speed of 28 mm/min. The wear rate is also reduced to 5.5×10^{-6} gm/m from 7×10^{-6} gm/m by a significant grain refinement. The properties of composites are reduced by the increment of transverse speed through reduced grain refinements. The heat generation and stirring action of the tool are reduced by the addition of transverse speed which affects the strength of FSPed samples [120]. The grain refinement and the flow of material are directly related to the improvement of strength and wear resistance. However, the generation of frictional heat in the processed zone could control the grain reduction and material flow during FSP [127]. Hence, sufficient heat, nearly 60%–90% of melting temperature is required to refine grain in the metallic structure [38]. Moreover, the hardness of SZ can be decelerated by coarse grain growth on a further increment of frictional heat and reducing tool pin revolution on FSPed samples [112]. The SiC

particles are reinforced on the Al5052 sheet by FSP with different transverse speeds of 40, 80, and 125 mm/min. Microhardness improves by 55% at 80 mm/min traverse speed by refined grains, evenly distributed SiC particles, and a quench hardening effect [128]. The 8 vol% of 10 nm sized SiO_2 particles are reinforced on as-cast AZ91 magnesium alloy by FSP with varying transverse speeds of 20, 40, and 63 mm/min at a constant rotational speed of 1250 rpm. The FSPed samples exhibit a 124 HV microhardness, 193 MPa UTS, and 12.5% elongation attained by refined grain size in the SZ. The refined grains are achieved by increasing traverse speed due to the reduction of the heating effect in grain growth. High traverse speed reduces the duration of heat which limits the grain growth. The refined grains of 14.12 μm, 11.07 μm, and 8 μm are attained under 20, 40, and 63 mm/min transverse speed respectively (Fig. 14). The increment of traverse speed attributes minimum contact of the tool with the workpiece which effects the induced frictional heat that limits the grain growth [127].

FSP is used to refine the grain size of Al–Cu alloy under the different traverse speeds of 200, 300, and 400 mm/min at 1000 rpm rotational speed. A 62.9% grain reduction is attained in the SZ by increasing the traverse speed from 200 to 400 mm/min. The yield strength is increased by 1.4 times due to the uniform grain refinement in the SZ [129]. FSP is employed on SS430 to enhance microstructure, hardness, and wear behaviour at traverse speeds of 16, 40, and 60 mm/min with a constant rotational speed of 1400 rpm. A defect-free and uniform grain is achieved in the SZ under 16 mm/min. The defects such as grooves are observed on the processed zone under 40, and 60 mm/min due to the grain growth by the effect of heating. The grains are reduced by 4 times through dynamic recrystallization, frictional heat, and

severe plastic deformation by 16 mm/min traverse speed. The severe plastic deformation and rapid cooling attribute a fine martensitic structure in the ferrite grain boundary. A 64% hardness is enhanced on FSPed samples by the formation of martensite and grain refinements. The wear resistance is improved by 17.4 times by the effect of high hardness and fine-grain martensite structure in SZ [130]. FSP is used to improve the microstructure, UTS, and hardness of 2205 duplex Stainless Steel (SS). The better grain refinements are obtained on a minimum traverse speed of 12 mm/min which is attained a different traverse speed of 12, 16, 25, and 40 mm/min with a 1000 rpm rotational speed (Fig. 15). The evenly distributed fine grain structures are obtained in the SZ that enhances the UTS and hardness by 1097 MPa and 450 HV [131]. A 21.53 vol% of TiC particles are reinforced AZ61 magnesium composite by FSP with different traverse speeds of 25, 100, and 170 mm/min at a constant rotational speed of 850 rpm. The crack, pinholes, piping, voids, and tunnel defects are minimized by refined grains with homogenous distributions under 25 mm/min traverse speed. The increment of traverse speed attributes a lack of materials, tool stirring effect, and weld flaw [132].

3.1.3 Multi-pass FSP

The FSP could be completed by more than one pass of a tool in the same processed zone to achieve ultrarefined grains. The dislocation density and grain reduction of FSPed samples are improved by multi-pass of FSP. Moreover, multi-pass are conducted by the same direction or counter direction of the tool over every pass to produce homogenous dispersed grains on the base metal than single pass FSP [133–135]. The multi-pass FSPed samples exhibit HAGBs, more texture

Fig. 14 Microstructure of SZ. **a** 20 mm/min, **b** 40 mm/min, **c** 63 mm/min traverse speed [127]
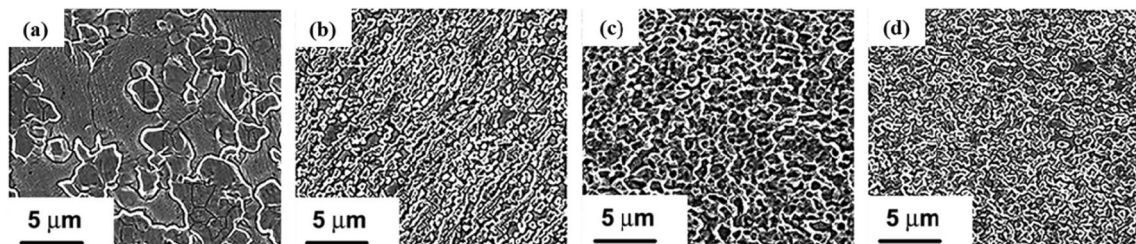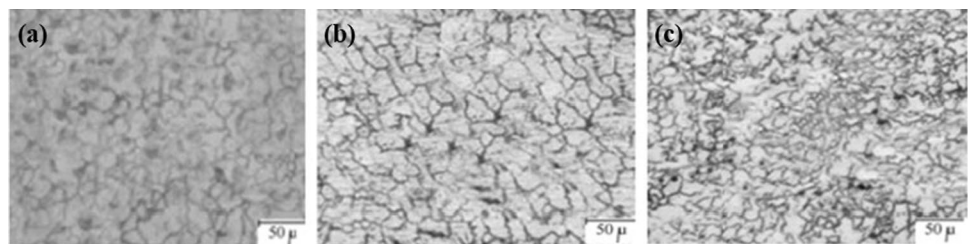
Fig. 15 Microstructure of SZ. **a** 40 mm/min, **b** 25 mm/min, **c** 16 mm/min, **d** 12 mm/min traverse speed [131]

is responsible for the transformation of β to α phase due to sudden temperature change and leads to the formation of Widmanstatten morphology structure [136]. Many research experiment results show that the mechanical properties and tribological behaviour are improved by using multi-pass FSP than single-pass [119, 137, 138]. The irregularly dispersed and uneven reduction of HEA particles is reduced by multi-pass of FSP in the processed zone [139, 140]. Mechanical properties are analyzed on SiO_2 particles reinforced AZ91 magnesium alloy under the effect of 1 pass, 2 passes, and 3 passes of FSP. Microhardness, UTS, and elongation of 3 passes FSPed samples increase by 15.8%, 44.5%, and 16.7% respectively due to the uniform distribution of refined grains in SZ as shown in Fig. 16. The multi-pass FSP attributes a homogenous grain distribution, severe grain refinements, quench hardening effect, minimizing porosity and voids, dissolved $Mg_{17}Al_{12}$ hard precipitates in grain boundaries that improve the mechanical properties [127].

The impact of multi-pass FSP is analyzed on AA6082-T6 by reinforcing SiC particles with a 1350 rpm rotational speed and 65 mm/min traverse speed. The SiC particles are evenly distributed with equalized refined grains that enhance UTS and hardness by 32.7% and 49.4% by dynamic recrystallization and the Zener- Holloman parameter. The UTS and hardness are observed as 223.61, 238.37, 255.63, 281.79, 296.86 MPa, and 89, 101, 119, 125, 134 HV by 1, 2, 3, 4 and 5 passes of FSP respectively. A homogenous dispersion, material mixing and grains are reduced continuously as 25.27, 17.43, 12.87, 8.53, and 5.17 μm by increment of passes. The grain refinement and uniform dispersion of grains in the SZ depend on the induced frictional temperature. The dispersion of SiC particles, reduction of agglomeration of SiC, and defects are enhanced by 5 passes FSP than the single pass (Fig. 17) [141]. TiC particles are reinforced on Al–Zn–Mg–Cu alloy by multi-pass FSP with 1150 rpm rotational speed and 60 mm/min traverse speed. The hardness, tensile strength, and surface roughness of 208.64 HV, 484 MPa, and 153.593 nm are attained due to the evenly distributed grain refinements, formation of strain field, hindering of particle agglomeration, and dislocations mobility after 6 passes of FSP [142]. The UTS and yield strength of the FSPed Cu sample is improved after 4 passes through grain refinements. A 215 MPa UTS, 200 MPa yield strength, and 800 nm sized grains are obtained through 4 passes FSP by strain hardening, frictional heat, a higher fraction of HAGBs, dramatic grain size reduction, and reduced dislocation densities [143].

Multi-pass FSP employed on CoCrFeMnN HEA base to improve the homogeneity and grain refinements by the effect of nitrogen alloying. Nitrogen alloyed (N1) multi-pass FSP exhibits a more refined grain structure than that of nitrogen-free (N0) FSPed samples. The Inverse Pole Figures (IPF) with Average Grain Size (AGS) of the processed zone under different passes of FSP as shown in Fig. 18. The N1-first pass FSP is more evenly dispersed (Fig. 18d) than N0-first pass FSP (Fig. 18a). Moreover, on increasing

Fig. 16 Microstructure of SZ. **a** One pass, **b** Two passes, **c** Three passes of FSP [127]
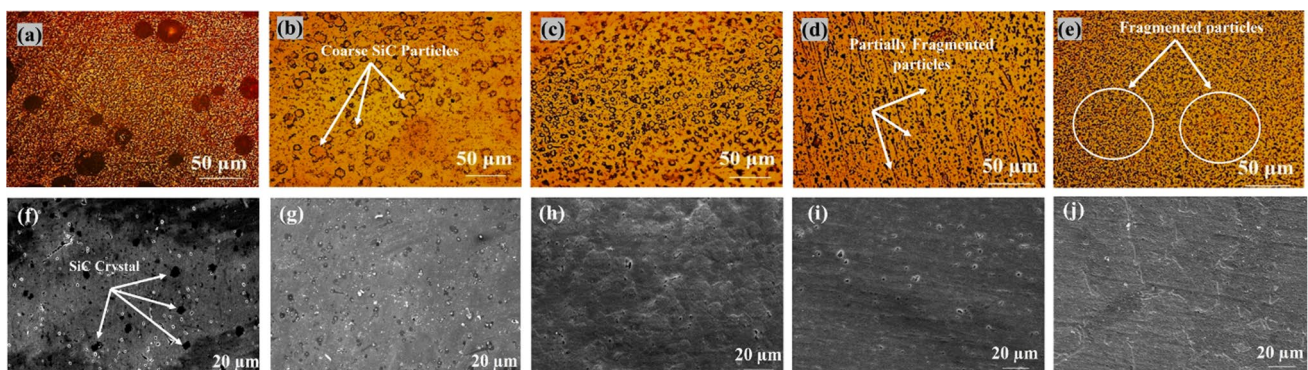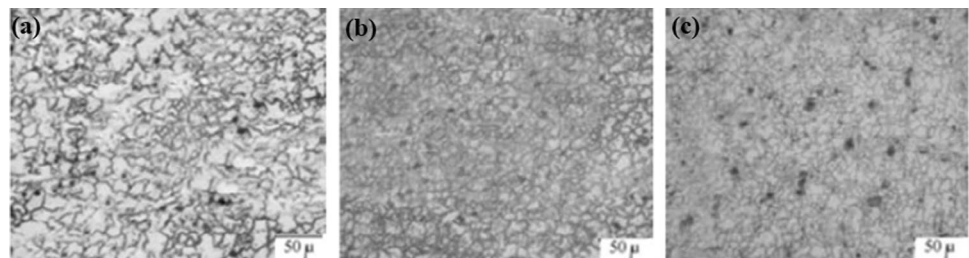
Fig. 17 Optical microscopy and SEM images. **a, f** One pass, **b, g** Two passes, **c, h** Three passes, **d, i** Four passes, **e, j** Five passes of FSP [141]

Fig. 18 IPF maps of grain reduction with AGS. **a** N0–1 pass FSP, **b** N0–2 passes FSP, **c** N0–3 passes FSP, **d** N1–1 pass FSP, **e** N1–2 passes FSP, **f** N1–3 passes FSP [140]
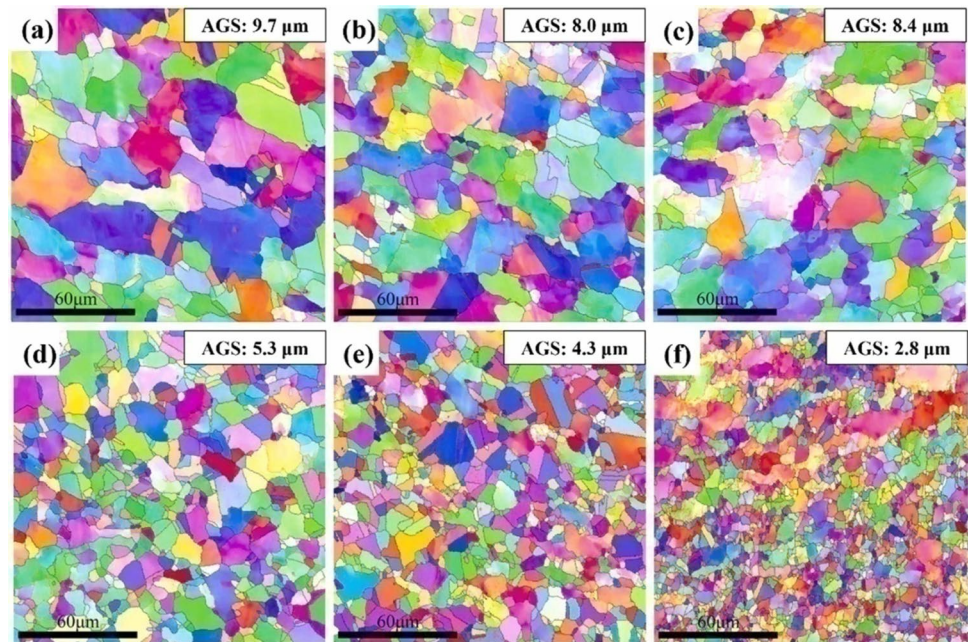
the passes of FSP on samples, a further reduction in grain size is obtained (Fig. 18b, e). Finally, the optimum AGS of 2.8 μm is obtained by N1 than the N0 after 3 passes of FSP (Fig. 18c, f). The multi-pass FSP plays a major role in grain refinement with homogeneous distribution on the base metal. In addition, the effect of nitrogen alloying is beneficial for continuous dynamic recrystallization and even dispersion of HEA elements on the base metal [140].

3.1.4 Axial Force

The axial force is one of the parameters that is given to the tool towards the workpiece in a downward direction during FSP. The axial force influences the generation of frictional force between the tool and the workpiece. The induced frictional force increases with the increment of axial force [120]. FSP is employed on AA6063-T6 aluminum alloy to improve hardness and UTS under varying axial forces 8, 10, and 12 kN. Axial force plays a vital role in induced frictional heat during FSP which influences the refined grains through plastic deformation and recrystallization. The insufficient heat attributes a poor material flow and stirring action of the tool by lower axial force which leads to defects that minimize the mechanical properties. However, microvoids and tunnel defects are induced by the excessive heat generated through higher axial force. The defects-free surfaces are obtained by sufficient frictional heat and hydrostatic pressure in the SZ by optimal axial force. The hardness and UTS increase by 33.4% and 46.5% under the effect of severe plastic deformation and significant material flow by 10 kN axial force [144].

3.1.5 Tilt Angle

The tilt angle prevents wear due to the excessive generation of frictional heat caused by the contact between the tool and the workpiece. The tilt angle provides easy movement of the tool during the FSP and influences the homogenous distribution and refined grains over the base metal. In general, the angle provided to tool is in the range of 0–3° [120]. SiC particles are reinforced on AA6061 composites to improve microhardness under the different tilt angles 1.5, 2, and 2.5°. The enhanced microhardness of 116 HV is obtained under the 2.5° tilt angle at 1400 rpm rotational speed and 50 mm/min traverse speed which is 23.4% higher than the base metal. The severe plastic deformation and sufficient heat generation under the combined process parameters lead to an evenly distributed uniform grain structure [145]. The effect of various machining parameters such as rotational speed, traverse speed, axial force, number of passes, and tilt angles on grain size and mechanical properties are numerically tabulated in Table 2. The mechanical properties of FSPed samples are improved by the grain refinements under the machining parameters. Hence, the machining parameters are directly affecting the strengthening mechanism.

3.2 Effect of Tooling Parameters on Microstructure and Mechanical Properties

The tool plays a major role in improving properties through severe plastic deformation and dynamic recrystallization due to the induced frictional heating. The mixing and homogenous distribution of refined reinforcement particles with base metal is essential to produce a strengthening mechanism.

Table 2 Various machining parameters used in FSP by previous research work

| Materials	RS* (rpm)	TS* (mm/min)	Axial force (kN)	No. of pass	Tilt Angle (°)	Grain size (µm)	Hardness (HV)	UTS (MPa)	YS* (MPa)	Refs.
A356+Si	300, 500, 700, 900	51, 102, 203	–	1	–	3–4	–	–	–	[39]
NAB+Cr	710, 1000, 1400	28, 40, 56	–	4	–	6.3	385	701	330	[120]
A319 alloy	800, 1000, 1200, 1400, 1600	22.2, 40.2, 75	–	1	–	–	110	221	191	[122]
Pure Al+Si	500, 700, 1000	15, 20, 30	–	1	2	–	150	–	84	[123]
A5083+fullerene	500, 1000, 1500, 2000	50	–	1	3	0.2	143	–	–	[124]
AZ61+Al$_2$O$_3$	800, 1000, 1200	45	–	4	2	1–5	85–92	–	–	[126]
AZ91+SiO$_2$	1250	20, 40, 63	–	3	3	8	124	192	–	[127]
Al5052+SiC	700, 1120, 1400	40, 80, 125	–	4	3	0.9	116	–	–	[128]
Al-Cu alloy	1000	200, 300, 400	–	2.5	1	0.12	105	–	55	[129]
SS430	1400	16, 40, 60	30	3	1	10.5	328	–	–	[130]
2205 duplex SS	1000	12, 16, 25, 40	40	1	–	–	450	1097	–	[131]
AZ61+TiC	850	25, 100, 170	–	4	3	–	–	–	–	[132]
AA6082-T6	1350	65	7.2	5	2	5.17	134	296.86	–	[141]
Al–Zn–Mg–Cu alloy+TiC	1150	60	–	6	–	2.4	208.64	484	–	[142]
Cu	630, 1600	40, 315	–	4	2	0.8	–	215	200	[143]
AA6063-T6	800, 1000, 1200, 1400, 1600	22.2, 40.2, 70	8, 10, 12	1	–	–	114 kg/mm^2	331	217	[144]
AA6061+SiC	900, 1120, 1400	31.5, 40, 50	–	1	1.5, 2, 2.5	–	116	–	–	[145]
Al+TiC	640, 800, 1000	60, 120, 150	–	1	–	9	48	163	–	[125]
Ti+SiC	600, 800, 1000, 1250, 1400, 1600	25, 35, 45, 55, 65	–	4	–	0.4	534	–	–	[146]
Fe$_{42}$Mn$_{28}$Co$_{10}$Cr$_{15}$Si$_5$	150, 350	50.8	–	3	–	1	–	1850	–	[147]
Fe$_{40}$Mn$_{20}$Co$_{20}$Cr$_{15}$Si$_5$	150, 350	50.8	–	2	2	0.5–0.6	–	1130	784	[148]

*RS rotational speed, *TS* traverse speed, *YS* yield strength

These aspects could be controlled by the stirring action of the tool during FSP. Many tools are available with different shapes and tool pin profiles such as cylindrical, square, conical, and triangular shapes with or without threaded as illustrated in Fig. 19 [119, 149]. Depending upon the reinforcement and the base metals used in FSP, the tool selection is made. The effective material flow and generation of friction heat are influenced by the geometry and shape of the tool pin [150]. Several materials are used for tools in FSP such as HSS, H13 steel, tool steel, tungsten carbide, PCBN, W–Re alloy, and Inconel [119]. The tool may be consumed due to the induced wear during FSP by insufficient strength of tool materials. The selected tools are eco-friendly to manufacture, easily available, non-consumable, and should be harder than work materials, withstand the axial force and friction [45].

The H13 with 53 HRC hardness tool is used to reinforce alumina particles on AZ31 by FSP. Three different tool profiles such as columnar probe without threads, columnar probe with threads, and columnar probe with threads along three flutes are used. The non-threaded and three-flute tool processed samples are observed with cavities and micro-voids due to the insufficient material flow over the SZ (Fig. 20). The even distribution of grains in the SZ exhibits under the tool with the threaded type [126]. The microhardness and surface roughness are analyzed on FSPed Al6063 alloy under the two different tool pin geometries such as cylindrical threaded and the taper threaded pins at 1150 rpm rotational speed and 50 mm/min traverse speed. The tapper threaded pin offers enhanced microhardness and surface roughness than the cylindrical threaded pin through refined grains with homogenous distribution. The microhardness and surface roughness are improved by 62.1 HV

and 2.71 μm under the tapper threaded pin due to the material flow, dense precipitate distribution, and formation of equiaxed grains by dynamic recrystallization [151]. FSP is used to reinforce B_4C particles on AA7075 alloy by pinless and conical pin tools with 400 and 600 rpm rotational speed at a 50 mm/min traverse speed. The enhanced hardness of 151.5 HV is observed under the conical pin tool over the pinless tool through effective dispersion of B_4C particles over base metal, homogenous distribution of grains, and dynamic recrystallization [152]. The effect of tool geometry analyzed on FSPed AA2024-T351 under threaded cylindrical and triangular pin profiles with 1000, 1200, and 1400 rpm rotational speed at a 100 mm/min traverse speed. Significant grain refinements, homogenous distribution, and defect-free surfaces are attained under the triangular pin tool that improves the microhardness by 140 HV. The insufficient plastic deformation and materials flow due to the lack of heating effect by stirring action of the tool leads to the formation of voids and cavity attributes minimum hardness under threaded cylindrical pin tool [153].

FSP is used to reinforce Ni particles on Al5053 alloy by two different tool geometries such as cylindrical plain tool and threaded pin with spiral groove tool. The hardness, yield strength, and UTS are improved by 91 HV, 184 MPa, and 339 MPa by threaded pin with spiral groove tool over plain tool due to the effective material flow and sufficient plastic deformation by induced frictional heat. The tunnel defects and agglomeration of coarse Ni particles are observed in the processed zone by plain tool due to the lack of heating and material flow (Fig. 21a, b). However, a fine grain structure of 3 μm is distributed homogenously with effective mixing and material flow that improves the strength of FSPed samples by the modified tool (Fig. 21c) [154]. Al_2O_3–TiB_2 particles
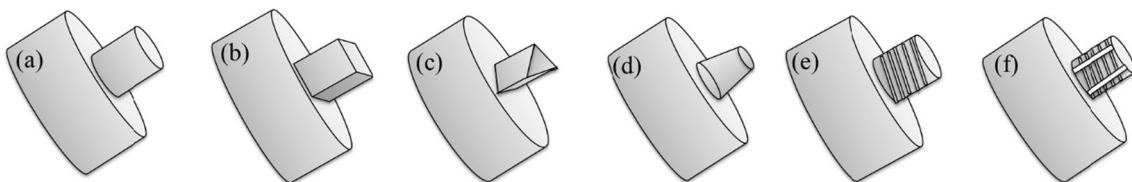
Fig. 19 Geometry of tool pin profiles. **a** Cylindrical, **b** Square, **c** Triangular, **d** Conical, **e** Threaded columnar, **f** Threaded columnar with flutes

Fig. 20 Macrostructure of the SZ region. **a** Probe without threads, **b** Probe with threads, **c** Probe with threads along three flutes [126]
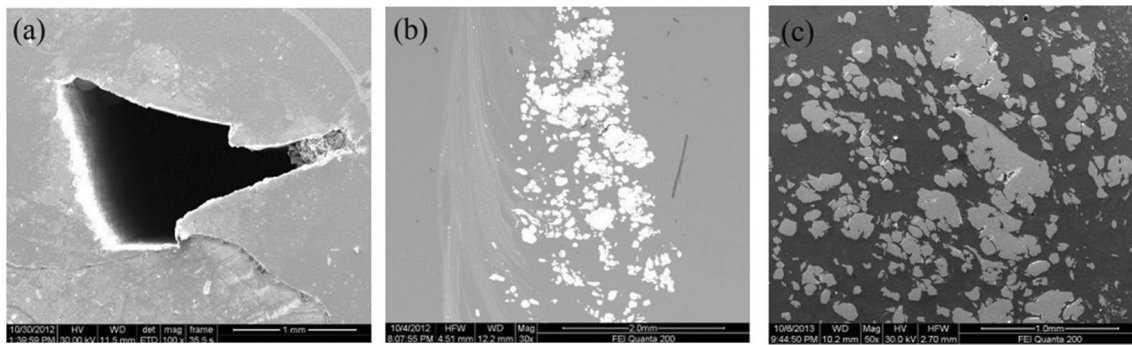
Fig. 21 SEM images. **a** Tunnel defect, **b** Agglomeration of Ni particles under cylindrical plain tool, **c** Dispersion of Ni particles under modified tool [154]

are reinforced on Al6061 by FSP with different tool pin profiles such as cylindrical, threaded cylindrical, taper, square, and triangular at 1500 rpm rotational speed, 25 mm/min traverse speed, and 3° tilt angle. The square and triangular pin profiles attribute more equalized grains by the effective stirring action of the tool. The processed zone exhibits an average grain size of 2.4, 2.3, 1.8, 1.2, and 1.1 μm by straight cylindrical, taper cylindrical, threaded cylindrical, triangular, and square respectively. Subsequently, a significant grain reduction and homogenous distribution with uniform grains appear by square and triangular pin profiles through severe plastic deformation and dynamic recrystallization through sufficient frictional heating [155]. FSP is employed to reinforce SiC particles on AA6063 through various pin profiles such as plain and tapered cylindrical, triangular, and square pin tools, cylindrical and square pin profiles with Clockwise (CW) and Counterclockwise (CCW) scrolled shoulder design. The rotational speed of 900 rpm, traverse speed of 40 mm/min, and title angle of 2.5° are used for significant process. The effective process obtained by the square pin tool under the flat shoulder design. The even distribution of uniform-sized grains with defective surfaces are attained by the CCW cylindrical pin profile due to the sufficient heating and stirring action of the tool [156].

FSP is employed to reinforce a 10 μm size SiC powders on Al6061 by the effect of increasing Tool Plunge Depths (TPD) by 0.10, 0.15, 0.20, 0.25, 0.30, and 0.35 mm on threaded cylindrical pin at 1400 rpm rotational speed and 40 mm/min traverse speed with 2.5° tilt angle. The formation cavity due to the insufficient heat generation by lower plunge depth, ejection of SiC powders with defects appeared on higher plunge depth. The evenly distributed equalized grains are obtained in the processed zone by optimum plunge depth. A 0.10 mm TPD exhibits a cavity in large size at the SZ center and cavity decreases with dispersion on SiC powders are observed under 0.15 mm TPD by enhancement of material flow (Fig. 22a, b). The uniform dispersion of SiC particles obtained by further increment of TPD by 0.20 mm

(Fig. 22c). A defect-free homogenous dispersion of SiC particles attained due to the addition of TPD by 0.25 mm (Fig. 22d). The further increment of TPD by 0.25 mm and 0.30 mm attributes to defects formation and uniformity of powder dispersion decreased due to excessive heat generation that leads to more softening of material around the tool surfaces (Fig. 22e, f) [157]. The Ti6Al4V particles are reinforced on Al1100 alloy by FSP with two different tool geometries of tool such as threaded taper and square shape pin tool. A 1200 rotational speed, 30 mm/min traverse speed, and 2.51° tilt angle with 3 passes FSP improves the wear resistance by 50% by threaded taper pin profile. The threaded taper pin profile attributes a significant distribution of Ti6Al4V particles due to the sufficient induced frictional heat by stirring action of the tool, grain refinements, and homogenous distribution with reduced agglomeration leads to enhanced mechanical properties by 79.78 MPa yield strength, 125.40 MPa UTS, 66.12% elongation, and 41.5 HV hardness [158]. The influence of tool materials, plunge depth, and tool pin profile on grain size, hardness, UTS, and yield strength of FSPed samples are presented in Table 3. The summarized data provides detailed information to the researchers on tooling parameters and their range for strengthening processed samples.

4 FSP on HEA Base Samples

The synthesized HEA samples are more sustainable via improved mechanical properties, wear and corrosion resistance by FSP. The FSP could not be used to change the initial shape of the HEA elements [42]. The refined grains are obtained by FSPed HEA samples contributing to further improvement of strength and strain hardening through precipitation and solid solution strengthening [115, 169]. The ultrafine grain structures are caused by the features of recrystallization. The grain size increased by induced frictional heat and that is hindered by the reinforced HEA particle. The
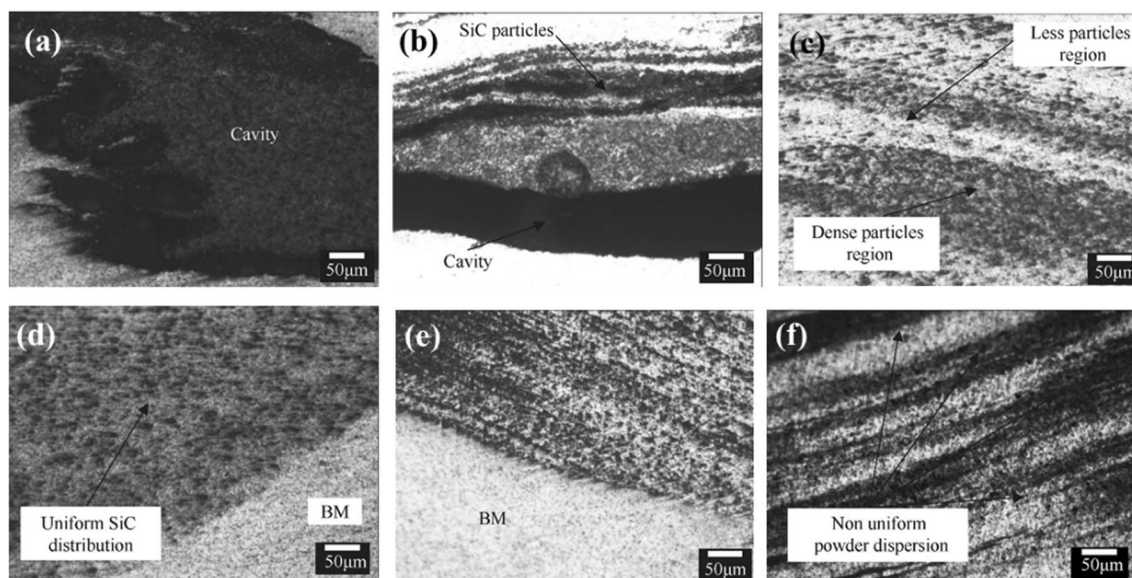
Fig. 22 Microstructure of the SZ region. **a** 0.10 mm, **b** 0.15 mm, **c** 0.20 mm, **d** 0.25 mm, **e** 0.30 mm, **f** 0.35 mm of TPD [157]

nucleation effects of HEA particles by continuous stirring action of the tool lead to the reduction of grains. Moreover, the quenching effect also contributes to refined grains by coefficient thermal expansion difference in HEA particles with base metal [56, 170].

4.1 Mechanical Properties of FSP on As-cast HEA Samples

The HEA samples demonstrate remarkable mechanical properties by FSP through ultrarefined grain structure, HAGBs, and low stacking fault energy at ambient and elevated temperatures. The refined grains of HEA are obtained by severe plastic deformation [171]. The Vacuum Induction Melting (VIM) synthesized $Al_{0.1}CoCrFeNi$ HEA sample is processed by FSP. The processed sample exhibits a single-phase FCC structure. Microhardness and yield strength are increased by 37%, and 110% than the as-cast HEA. The fine equiaxed grains of polycrystalline behaviour induced in a processed zone, HAGBs strengthening, and lattice friction stresses are attributes for higher microhardness and strength [54]. FSP with a WC tool employed on $Al_{0.1}CrCoFeNi$ HEA sample by submerged liquid cooling environment reveals an improved hardness and yield strength by 1.7 and 2.1 times than as-cast HEA. The low value of strain hardening exponent leads to efficient grain boundary strengthening and impedes the dislocation motion with BCC structure which is evidence for improved strength [172]. FSP is used to enhance the properties of the $Al_xCoCrFeNi$ HEA sample by incorporating Al powder and offering an increased UTS and yield strength by 1.85 and 3.4 times over the base metal. However, 28% of elongation decreases with the addition of Al powder to

HEA and evenly distributed elements in the Al regions as shown in EDS elemental mapping (Fig. 23a). HEA is finding a supplement grain refinement, BCC phase of Al with HEA element, and Al-rich precipitates [173].

The influence of nitrogen alloying on the VIM of CoCrFeMnNi HEA sample by FSP exhibits an improved UTS, yield strength, and elongation by 49%, 74%, and 32.6% respectively over as-cast HEA. The nitrogen alloy leads to refined grains by higher nucleation rate and retarding grain growth through dynamic recrystallization as shown in the Electron Backscatter Diffraction image (EBSD) (Fig. 23b). The impediment of dislocation movement is carried by super-saturated nitrogen atoms by FSP [115]. Multi-pass FSP employed with the W–Re alloy tool to evaluate the impact of nitrogen alloying on CoCrFeMnNi HEA samples exhibits an increase by 13.7%, 23.5% of UTS, and yield strength over free nitrogen alloying HEA. However, 33% of elongation is reduced due to the higher fraction of low angle boundaries, thermal stability, and ultrarefined grain size of 2.8 μm by multi-pass FSP as shown in EBSD (Fig. 23c) [140]. The VIM is used to synthesize $Fe_{49.5}Mn_{30}Co_{10}Cr_{10}C_{0.5}$ HEA samples and is processed by multi-pass FSP with $W-La_2O_3$ tool to increase hardness, yield strength, and UTS by 56.7%, 50%, and 15.2% respectively than the as-cast HEA. However, the elongation of FSP-processed HEA samples is decreased by 18% over as-cast HEA. The reduction of grain size by dynamic recrystallization and the Transformation Induced Plasticity (TRIP) effect induced FCC to the HCP phase through multi-pass FSP [174]. FSP used on the $AlCoCrFeNi_{2.1}$ HEA sample exhibits an increased micro-hardness, tensile strength, and ductility by 50%, 36%, and 3.5% respectively over as-cast HEA. The

Table 3 Various tooling parameters used in FSP by previous research work

Materials	Tool material	Plunge depth	Pin profile	Grain size (μm)	Hardness (HV)	UTS (MPa)	YS* (MPa)	Refs.
Al+TiC	M2 tool steel	–	Cylindrical	4	58	172	–	[37]
5083 Al	H13 tool steel	–	Cylindrical	1.6	–	–	–	[50]
Al6063	HSS	0.5	Cylindrical, Threaded taper	4	62.1	–	–	[151]
AA7075+B_4C	X210Cr12 tool steel	–	Conical	5	151	–	–	[152]
AA2024-T351	D2 tool steel	–	Threaded cylindrical, Triangular	–	140	–	–	[153]
Al5053+Ni	hardened steel	–	Cylindrical, Threaded—spiral groove	3	91	339	184	[154]
Al6061+Al_2O_3–TiB_2	H13 steel	–	Cylindrical, Threaded cylindrical, Taper, Square, Triangular	1.1	138	–	–	[155]
AA6063+SiC	HCHCr steel	–	Cylindrical, Tapered cylindrical, Triangular, Square	4.5	–	–	–	[156]
Al6061+SiC	H13 tool steel	0.10, 0.15, 0.20, 0.25, 0.30, 0.35	Threaded cylindrical	2.1	–	–	–	[157]
Al1100+Ti6Al4V	HSS	–	Threaded taper, Square	–	41.5	125.40	79.78	[158]
SS316	Tungsten carbide	0.35	Cylindrical	0.1–0.2	–	–	–	[159]
Cu+FeMnCoCrSi	W–Re alloy	3.85	Tapered cylindrical	–	–	–	0.77	[160]
$Fe_{40}Mn_{20}Co_{20}Cr_{15}Si_5$	W–Re alloy	3.65, 3.70	Tapered cylindrical	–	–	500	–	[161]
AZ61 Mg alloy+SiO_2	–	–	Cylindrical	0.5–2	105	–	–	[162]
Mg	H13 tool steel	0.1, 0.2, 0.3	Triangular	–	46	–	–	[163]
Al6061	MS tool		Cylindrical	1	69	–	–	[164]
AA5052	HCHCr	–	Pentagonal		69	215	–	[165]
AA6061-T6+SiC	HSS	–	Tapered cylindrical	–	–	189	–	[166]
Cu	H13 steel	–	Cylindrical, Square	0.33	89	257	223	[167]
AA7075	H13 steel	0.5	Triangular, Square, Circular	–	136	–	–	[168]

YS yield strength

ultrarefined grains are formed by the deformation of lamellar B_2 phase, FCC (L12) Cr, and Al-rich precipitate due to severe plastic deformation during FSP on the HEA sample (Fig. 23d) [114]. The vacuum arc remelted AlCoCrFeNi$_{2.1}$ HEA sample is processed by FSP with 3 wt% of TiO_2 nanoparticles. The hardness, yield strength, and shear strength are increased by 61.1%, 30.5%, and 23.7% respectively over as-cast HEA. The excellent grain refinement is found due to the dynamic recrystallization, broken and distributed B_2 phase, and rich Cr on the matrix. Moreover, the pinning effect of TiO_2 is also responsible for the improvement of refined grains in the FSPed sample as illustrated in the SEM image (Fig. 23e) [175]. A 3 wt% of SiC nano-particles are added to vacuum arc remelting of AlCoCrFeNi$_{2.1}$ HEA and FSP used to exhibit a 74.8% and 18% of microhardness and shear strength over as-cast HEA. The refined grains with reinforced SiC nano-particles and Zener pinning effect are attributed to higher strength through augmentation of grain
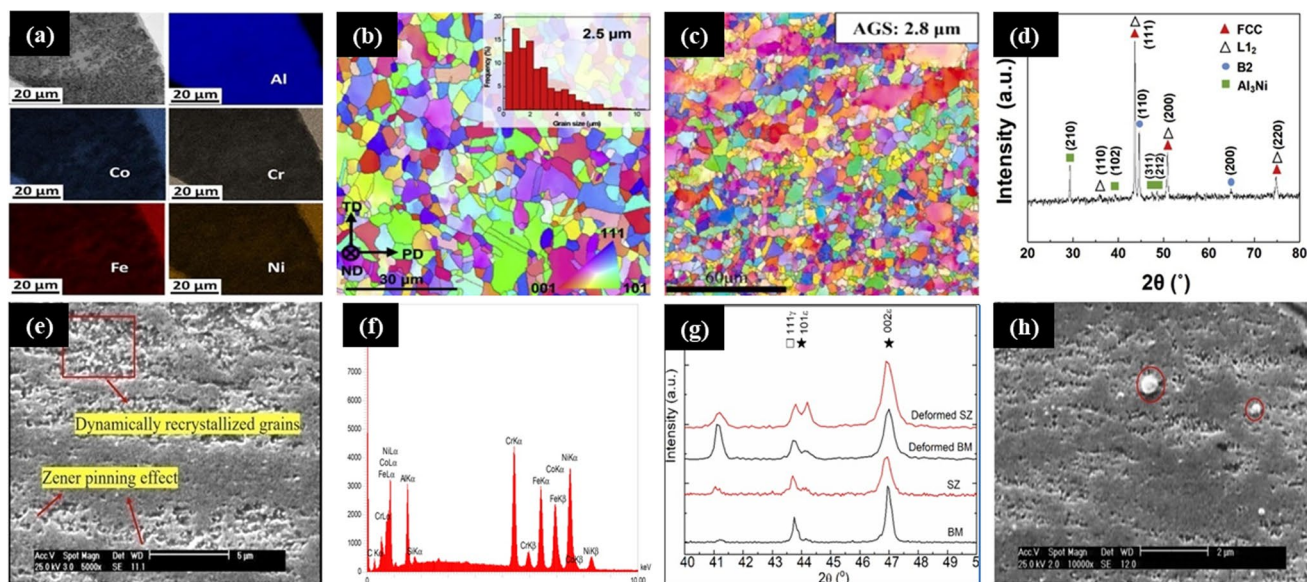
Fig. 23 a EDS elemental mapping of Al regions [173], **b** EBSD image of N1-FSP/ CoCrFeMnNi HEA, [115], **c** EBSD image with AGS in the processed zone after 3 pass FSPed CoCrFeMnNi HEA [140], **d** XRD analysis of FSP/AlCoCrFeNi$_{2.1}$ HEA [114], **e** SEM image—Zener pinning effect [175], **f** EDS image of surface nano-composites by FSP/AlCoCrFeNi$_{2.1}$ HEA [36], **g** XRD patterns of FSP/Fe$_{42}$Co$_{10}$Cr$_{15}$Mn$_{28}$Si$_5$ HEA samples [178], **h** SEM image of agglomerated particles [175]

refining and evenly distributed HEA particles on the SZ than thermo-mechanically affected zone (Fig. 23f) [36].

The CoCrFeNiCu HEA sample is processed through FSP to obtain an improved hardness, yield strength, and tensile strength by 150%, 187%, and 91.6% respectively to as-cast HEA. The coarse two-phase structures transformed into single-phase ultrarefined grain structures by segregation of Cu. In contrast, 5.2% of ductility is decreased, inferring that HAGBs, nano-scale twining deformation, low stacking fault energy, lattice distortion effect along with severe plastic deformation during FSP [171]. The vacuum arc melted TRIP HEA Fe$_{40}$Mn$_{20}$Co$_{20}$Cr$_{15}$Si$_5$ sample is refined by Friction Stir Gradient Alloying (FSGA) showing an increased modulus of 46.4% by the addition of Cu element over the as-cast HEA. The stabilization of γ phase and supersaturation of Cu on the matrix are responsible for higher modulus even grain growth by FSGA [176]. The VIM-synthesized CrMn-FeCoNi HEA sample is processed by FSP with the WC-12 Co tool to enhance the results. A 76.5% hardness value is increased on the shear processed zone over the as-cast HEA due to extremely high fine grains of 0.97 μm with relative grain refinement, high degree of refinement, and dislocation densities as per the Hall-Patch relation [55]. FSP with W–Re stir tool is employed on the CoCrFeMnNi HEA sample fabricated by laser powder bed fusion demonstrating an increased elongation, and UTS by 37.5% and 8.4% over as-cast HEA. However, hardness and yield strength are reduced by 36.4%, and 11% due to insufficient temperature distribution, friction heating, and uneven material flow during

FSP. Hence, inadequate strength is obtained on SZ than the base metal [177]. The vacuum arc cast Fe$_{42}$Co$_{10}$Cr$_{15}$Mn$_{28}$Si$_5$ HEA sample is processed through FSP with the W–Re tool. The γ-phase FCC and ε-martensite HCP phase structures are obtained in the XRD pattern as shown in Fig. 23g. The decreased ε-martensite phase and discontinuous dynamic recrystallization in the SZ lead to a slight decrement in yield strength than the as-cast HEA [178].

4.2 Wear and Corrosion Behaviour of FSP on As-cast HEA Samples

The single-phase FCC structure, strain hardening, and improved ductility of FSPed HEA samples are credited to exhibiting higher wear and corrosion resistance. The dislocation interactions of fine grains, work hardening, and low stacking fault energy are to avoid pits and micro-cracks of HEA samples during corrosion environments. Moreover, an argon atmosphere is used to avoid oxidation during FSPed HEA samples to enhance corrosion resistance [172]. The FSP is used on a CrMnFeCoNi HEA sample exposed to ambient temperature with 0.5 M of Na$_2$SO$_4$ electrolyte solution. The higher stability is obtained by FSPed samples over base metal in open circuit potential. A Cr$_2$O$_3$ passive layer is formed rapidly on HEA particles and higher corrosion resistance is induced due to the ultrarefined grains on the FSPed sample. The polarization pits are predicted on HEA samples by the effect of micro-galvanic nature [55]. Al$_{0.1}$CrCoFeNi HEA sample is processed through FSP by WC tool with

submerged liquid cooling and reveals the morphology of samples. The reduction in micro-cracks and shallow pits are observed on the FSPed HEA sample. The erosion rate of the FSPed HEA samples decreased by 20% due to increased hardness by refined grains and better resistance to plasticity along with a high volume of BCC structure [172]. FSP is employed on the AlCoCrFeNi$_{2.1}$ HEA sample with the addition of 3 wt% of TiO$_2$ nano-particles and the wear rate is recorded to be increased by 60% due to the agglomeration and incoherency of TiO$_2$ nano-particles with the matrix as shown in SEM image (Fig. 23h). During FSP a high temperature is produced by friction which leads to the initiation of an abrasive wear mechanism [175]. Table 4 describes the mechanical properties, wear, and corrosion behaviour of various combinations of FSPed HEA samples. The compressed data describes the detailed information of the previous experimentation works.

5 FSP on Al Alloys with HEA

In materials science and engineering, aluminium and its alloys have a high strength-to-weight ratio, owning to this property, Al alloys are employed in various industries like structural, transport, space industries, automobiles, and so on. To achieve enhancement in mechanical properties, wear and corrosion properties of Al, HEA particles are used as reinforcement for its unique performance. HEA with Al alloys through FSP used very recently exhibits various strengthening mechanisms such as grain size strengthening, solid solution strengthening, precipitation strengthening, and dislocation strengthening [179]. The Hall–Petch relation is ruled on grain size strengthening to obtain better mechanical

properties on FSPed HEA/Al alloys [112]. The FSP plays a major role in grain size refinement, equiaxed and homogeneously dispersed on AMCs, stimulated nucleation mechanism and impediment of grain growth, and grain boundary motion due to the elemental inter-diffusion and thermodynamic driving force [180, 181].

5.1 Mechanical Properties of FSP on Al Alloys with HEA

The enhanced results on mechanical properties of FSPed HEA/Al alloys mainly depended on grain size strengthening, Orowan strengthening mechanisms, and impeding dislocation movement. The HEA particles have high thermomechanical stability in the SZ and as evidenced by many kinds of research shows that the primary shape of HEA particles does not change even after multi-pass FSP [101]. AMCs with Al$_{0.8}$CoCrFeNi HEA particles are effectively accomplished by multi-pass FSP and the micro-hardness, yield strength, and UTS are increased by 56.1%, 42%, and 22% respectively over FSP/Al alloy. However, the elongation of FSPed AMCs is decreased by 30% due to the BCC phase of HEA particles (Fig. 24a). The reinforced HEA particles are to be identified on the bottom of dimples (Fig. 24b) [11]. The AlCoCrFeNi HEA particles are reinforced with 5083-AMC by a multi-pass of FSP. Microhardness is increased by 50% and 39.8% over base metal and FSPed composites due to the dislocation movement of HEA particles, grain size refinement, and different thermal contraction coefficients of HEA with AMCs by quench hardening effect. The enhanced results obtained on 5 passes of FSP implied the effective distribution of HEA particles with AMCs [182]. The Al$_{0.1}$CoCrFeNi HEA particles on 1060 Al alloy are

Table 4 Mechanical properties, wear, and corrosion behaviour of FSPed as-cast HEA samples

HEA particles	Hardness (HV)	YS* (MPa)	UTS (MPa)	EL* (%)	Wear rate (g/Nm)	Corrosion rate (μA/cm^2)	Refs.
AlCoCrFeNi$_{2.1}$	480	290	407 USS*	–	–	–	[36]
Al$_{0.1}$CoCrFeNi	132	315	–	–	–	–	[54]
CrMnFeCoNi	279	–	–	–	–	–	[55]
CoCrFeMnNi	–	493	832	32.6	–	–	[115]
AlCoCrFeNi$_{2.1}$	450	1360	–	10	–	–	[114]
CoCrFeMnNi	–	530	869	33	–	–	[140]
CoCrFeNiCu	380	1150	1150	5.2% ductility	–	–	[171]
Al$_{0.1}$CrCoFeNi	625	507	–	–	–	20%	[172]
Al$_X$CoCrFeNi	–	525	784	37	–	–	[173]
Fe$_{49.5}$Mn$_{30}$Co$_{10}$Cr$_{10}$C$_{0.5}$	254	437	818	18	–	–	[174]
AlCoCrFeNi$_{2.1}$	485	300	411 USS*	–	12.6E–7	–	[175]
CoCrFeMnNi	299	563	719	37.5	–	–	[177]
Fe$_{42}$Co$_{10}$Cr$_{15}$Mn$_{28}$Si$_5$	–	–270	–	–	–	–	[178]

YS yield strength, *EL* elongation, *USS* ultimate shear strength
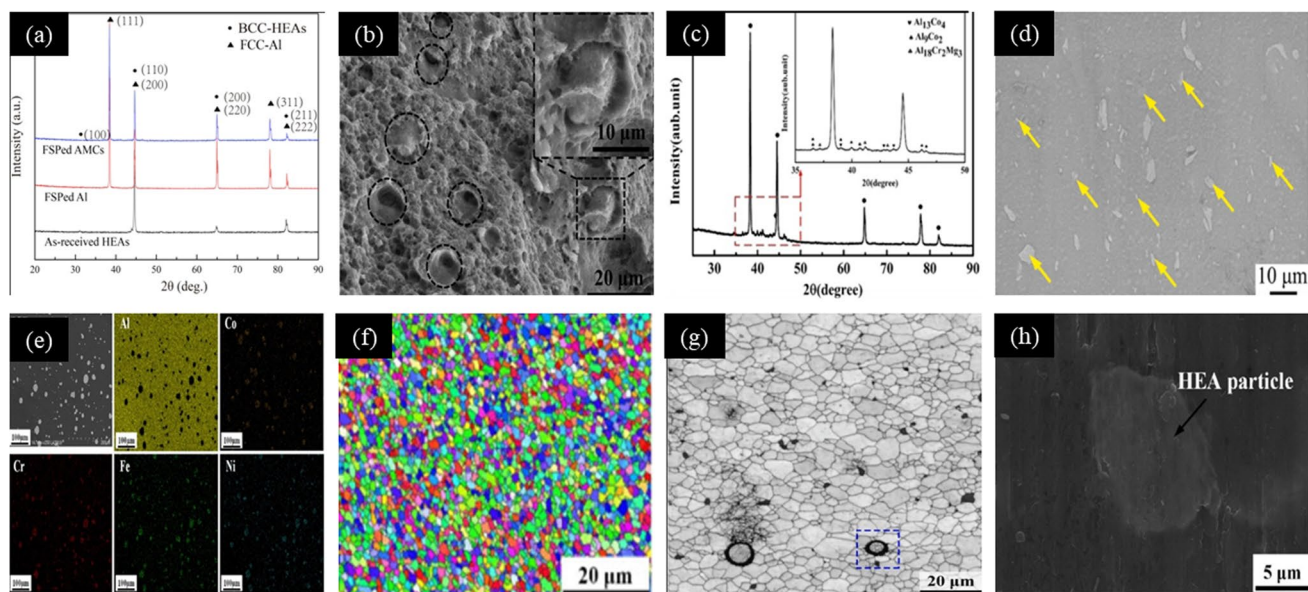
Fig. 24 **a** XRD patterns of FSPed $Al_{0.8}CoCrFeNi$ HEA/AMCs [11], **b** SEM image—Dimples formation in FSPed $Al_{0.8}CoCrFeNi/AMC$ [11], **c** XRD patterns of FSPed AlCoCrFeNi HEA/AMCs [100], **d** SEM image of micro-pores free surface [101], **e** EDS elemental mapping of FSPed AlCoCrFeNi HEA/AMCs [66], **f** EBSD image of FSPed AlCoCrFeNi HEA/AMCs [40], **g** SEM image—PSN effect on FSPed CrMnFeCoNi HEA/AMCs [8], **h** Cracks free worn surface of UFSPed AlCoCrFeNi HEA/AMCs [40]

processed by FSP and the impact of Al addition is evaluated. The hardness of HEA-processed samples is increased gradually with an increment of Al compositions. Due to the natural heat treatment of FSP, the heat-affected zone, and thermo-mechanically affected zone are harder than the base metal. Moreover, a much higher hardness is obtained in the aluminium addition zone due to comprehensive strengthening effects with Al alloy to HEA by FSP [183].

FSP is used to reinforce AlCoCrFeNi HEA particles with AMCs revealing high yield and tensile strength. The $Al_{13}(CoCrFeNiMg)_4$, $Al_9(CoFeNi)_2$, and $Al_{18}Cr_2Mg_3$ interface layers are formed and used to transfer the load to HEA from the matrix (Fig. 24c) [100]. HEA particles with AMCs are fabricated by Cold Spray (CS) and subsequently, FSP is used to improve the micro-hardness, and UTS by 91% and 60% through fine grain homogenization, densification, and minute interfacial diffusion over the CSed samples. Due to the high strength of AMCs, the elongation of FSPed samples is decreased by 17.5% over CSed samples. The CSed samples have several micro-pores in the Al matrix and are eliminated on the FSPed sample by PSN effects as shown in Fig. 24d [101]. More recently, submerged FSP is used to reinforce AlCoCrFeNi HEA particles on AMCs to impede the grain growth by evenly dispersed elements as shown in the EDS plot (Fig. 24e). The yield strength and UTS are increased by 25.1%, and 31.9% than the base metal and upheld by 18.9% significant ductility. Severe interfacial reactions are developed for the improvement of interface bonding strength between HEA and AMCs [66]. The

cooling-assisted FSP is employed with a different percentile of HEA-AlCoCrFeNi with AMCs. Refined grains and interface bonding of 15% HEA with AMCs are responsible for producing a microhardness of 65.9% higher than the base metal [184]. The impact of AlCoCrFeNi HEA particles with AMCs by underwater FSP is investigated through a nano-indentation test. The improved microhardness and modulus are obtained over base metal by minimizing the penetration. Hall–Petch strengthening, broken of HEA particles and nano size broken $Al_6(Mn, Fe)$ inter-metallic compounds attributed by Orowan strengthening. The fine grins appeared on HEA-reinforced AMCs by underwater FSP (Fig. 24f) [40]. CrMnFeCoNi HEA particles reinforced with 1060-AMCs through rotation friction extrusion process exhibit a 60% UTS increase and 39.4% elongation decrease due to the excellent plasticity and high dislocation dynamic recovery rate by PSN effects as illustrated in Fig. 24g. Inter-diffusion layer has ~ 7.35 GPa hardness, which is greater than HEA particles (~ 4.2 GPa) and matrix (~ 0.85 GPa) due to the synergistic of severe plastic deformation, adequate heat input, and excellent metallurgical bond with AMCs [8].

5.2 Wear and Corrosion Behaviour of FSP on Al Alloys with HEA

In the widening of Al alloy applications, it's necessary to find and improve wear and corrosion resistance. Powder metallurgy, squeeze, and stir casting are used in the past decade and these methods produced brittle inter-metallic

compounds in the interface. Hence, according to Archard's law, the enhancement of wear and corrosion resistance can be drawn by grain reduction through FSPed HEA/base metal [184]. FSP is one of the techniques to achieve refined equiaxed grains evenly dispersed on Al alloys and composites. The multi-pass FSP is employed on AlCoCrFeNi HEA particles with 5083-AMC and the optimum wear rate is obtained by 59.4% on 5 passes of FSP than the base metal. The multi-pass FSP is attributed to the moderate abrasive wear from the adhesive wear of base metal. The fine grains are uniformly dispersed over Al 5083 alloy, and fractured damage is prevented by higher microhardness [182]. The addition of AlCoCrFeNi HEA with AMCs through underwater FSP demonstrates more resistance to plastic deformation and inter-metallic compounds—$Al_6(Mn, Fe)$ holds the dislocation movement while sliding, and thereby wear rate is decreased by 48.6% than base metal. Due to the HEA particles, the micro-cracks, peeling-off, and delamination are suppressed as shown in the SEM image (Fig. 24h). The better metallurgical bonding, load bearing capacity by barrier effect of HEA particles with the matrix as evidence of cracks free worn surface [40].

The cooling-assisted FSP on 5083-O AMCs with a different percentile of AlCoCrFeNi HEA particles exhibit a 43% of wear rate, and 57.8% of weight loss, and the friction coefficient also decreased with the addition of HEA by Archard's law. Due to severe plastic deformation scratches, ploughs, and plastic flow are identified on base metal over FSPed samples. The irregular tearing ridges are reduced with an increment of HEA, obviously adhesive wear of base metal ends to abrasive wear [184]. FSP is employed on cold-sprayed CoCrFeNi particles with 6061-AMCs. The wear rate of FSPed samples is decreased by 51%, 81% at 25 °C (abrasion wear) 19%, and 82% at 200 °C (adhesion wear) respectively over CSed samples and base metal. The CSed samples immersed in 3.5 wt% NaCl solution shows cracks, micropores, and oxide films covered to HEA and formed a fine network structure with larger-sized holes for increasing the duration of immersion. The high wear and corrosion resistance are developed on FSPed samples by equiaxed refined dense grains evenly dispersed on AMCs due to dynamic recrystallization [185]. Table 5 presents the numerical values of improved mechanical properties, wear and corrosion resistance under the different constituent elements of HEAs reinforced to Al alloys through FSP. The summarized data provides detailed information on the FSP work in HEA with Al alloys and the research gap towards further experimental work.

6 FSP on Cu Alloys with HEA

The HEA particles are reinforced with Cu alloys by FSP to improve strength, hardness, and wear resistance instead of using nitrides, oxides, and carbides. HEA particles formed an interfacial bonding with the Cu alloy which generates a synergistic improvement in hardness, ductility, excellent wear, and corrosion resistance. The dynamic recrystallization, quench hardening, severe plastic deformation, Hall–Petch relationship, the rule of mixtures, HAGBs, and strain field between the HEAs and matrix attributes enhancement results in FSPed HEA/Cu samples [187, 188]. Moreover, controlling the dislocation motion through grain and twin boundaries also influences the improved strength in FSPed HEA/Cu samples [159].

Table 5 Mechanical properties, wear, and corrosion behaviour of FSPed Al alloy samples

| HEA particles	Hardness (HV)	YS* (MPa)	UTS (MPa)	EL* (%)	Wear rate (mm³/Nm)	Corrosion rate (µA/cm²)	Refs.
CrMnFeCoNi	–	–	160	39.4	–	–	[8]
$Al_{0.8}$CoCrFeNi	125.7	200	371	18.8	–	–	[11]
AlCoCrFeNi	135	–	–	–	7.55 E−4	–	[40]
AlCoCrFeNi	–	219	401	18.9	–	–	[66]
AlCoCrFeNi	–	16.8	28.1	15.3	–	–	[100]
CoCrFeNi	141	–	242	17.5	–	–	[101]
AlCoCrFeNi	158	–	–	–	1.6 E−6	–	[182]
AlCoCrFeNi	136	–	–	–	8.5 E−5	–	[184]
$Al_{0.1}$CoCrFeNi	600	–	–	–	–	–	[183]
AlCoCrFeNi	–	219	401	–	COF*–0.29	–	[186]
CoCrFeNi	193	–	–	–	0.62 E−6 @ 25 °C and 4.6 E−6 @200 °C	67.7	[185]

YS yield strength, *EL* elongation, *COF* coefficient of friction

6.1 Mechanical Properties of FSP on Cu Alloys with HEA

The enhanced mechanical properties of HEA particles with Cu alloy are obtained through single or multi-pass FSP by ultrarefined grains, dynamic recrystallization, and interfacial layer between HEA and base metal. According to the Hall–Petch relationship, higher hardness is obtained in the SZ than the thermomechanical zone, advancing side and retracting side due to induced frictional heat by FSP [104]. A 5–15 vol% of arc melting processed AlCoCrCuFe HEA particles are reinforced on the Cu base metal through FSP with the H13 steel tool. The addition of HEA particles leads to an increased hardness of 1.5 times over base metal. However, the UTS, yield strength, and elongation of FSPed samples are decreased which infers that the processed samples are more brittle, impediment the interface, and dislocation density [170]. FeCoNiCrAl HEA particles are incorporated into the Cu base metal by multi-pass FSP demonstrating an increased microhardness of 69.8% than the base metal due to the homogeneous dispersion of HEA particles by 3 passes of FSP which are shown in SEM image (Fig. 25a). Moreover, the Orowan mechanism, Hall–Petch relationship, and Zener pinning effect also aid the improvement of mechanical properties through ultrarefined grains. The dual structure of BCC and FCC phases are observed by HEA/Cu as shown in the XRD pattern (Fig. 25b). The FCC phase diffusion layer is formed at the interface and directed to ductile behaviour. Meanwhile, 87% of thermal conductivity is reached over base metal which leads to excellent thermal properties [189].

6.2 Wear Behaviour of FSP on Cu Alloys with HEA

The wear and corrosion resistance of the Cu alloy are increased by the addition of HEA particles through FSP. The wear resistance of HEA-processed samples increased by the barrier effect of the HEA particles during sliding [189, 190]. In addition, uniform fine grains are evenly distributed over base metal by multi-pass FSP, higher plastic deformation, and interfacial bonding exhibits a higher hardness. The high corrosion resistance is obtained by nano-grain structure through FSP to withstand severe plastic deformation on cavitations [159, 191]. The influence of AlCoCrCuFe HEA particles on the Cu base metal through FSP exhibits a decreased wear rate of 34.7% over base metal due to the load-carrying ability of HEA particles, the brittle nature of FSPed HEA samples, and adhesive wear tends to abrasive wear [170]. The multi-pass FSP is used to reinforce the CoNiCrAl HEA particles on the Cu base metal and a reduced wear rate of 29.7% over a base metal is observed. The adhesive wear mechanism is deteriorated by HEA particles due to the reduced contact area of the matrix with the counter plate. The grooves and pit-free surfaces are identified due to better interfacial bonding and evenly dispersed HEA particles over base metal as shown in Fig. 25c [189]. The reinforced HEA particles on Cu alloy by FSP and their enhanced mechanical and wear properties are presented in Table 6.
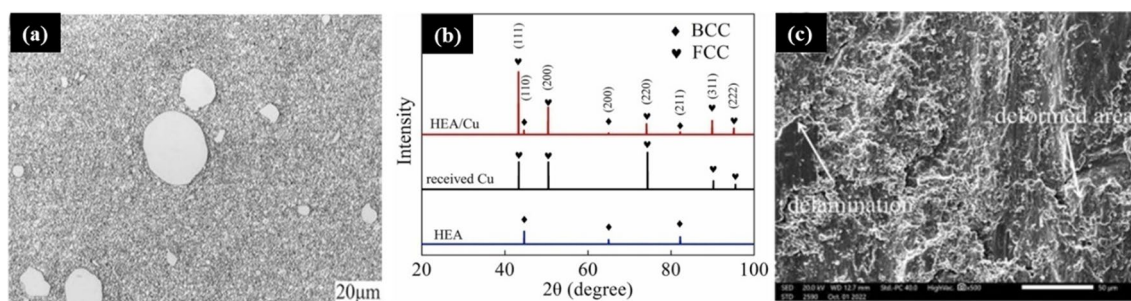
Fig. 25 **a** SEM image—after 3 passes of FSPed FeCoNiCrAl HEA/Cu [189], **b** XRD pattern of FSPed FeCoNiCrAl HEA/Cu [189], **c** SEM image—grooves and pit free worn surfaces [189]

Table 6 Mechanical properties, wear, and corrosion behaviour of FSPed Cu alloy samples

| HEA particles	Hardness (HV)	YS* (MPa)	UTS (MPa)	EL* (%)	Wear (g/Nm)	Refs.
AlCoCrCuFe	150	105	164	6.4	4.6 E−5	[170]
FeCoNiCrAl	212.54	–	280	30.66	1.5 E−6	[189]

YS yield strength, *EL* elongation

7 FSP on Stainless Steel Alloys with HEA

Stainless steel plays vital role in engineering industries for its strength, mechanical properties, and durability for various environments. The synergetic improvement of strength and ductility in SS is required to meet the current scenario. Hence, HEA is being used as reinforcement on the SS base metal through FSP for the enhancement of properties [65]. The microstructural modifications are observed on the surface of the SS base metal due to the refined grains by FSP. The superior strength is attained by dynamic recrystallization, planar defects—stacking faults, low angle boundaries, twining mechanism, inter-phase boundaries, and inhibiting dislocations. The FSPed samples exhibit excellent strengthening by grain refinement mechanism due to the higher value of the Hall–Petch coefficient and friction stress of HEA [54, 174, 192].

7.1 Mechanical Properties of FSP on Stainless Steel Alloys with HEA

The mechanical properties such as microhardness, UTS, flexural strength, yield strength, and elongation of FSP on SS base metals are improved by the addition of HEA. The interfacial bonding properties and hampering effect of HEA particles lead to the enhancement of the strengthening mechanism. A 17 μm ball-milled CoCrFeCuTi HEA is reinforced on SS304 by FSP through a WC tapper cylindrical tool. The microhardness and tensile strength of the HEA-processed sample are increased by 1.2 and 2.2 times of processed base metal by homogenously distributed refined grains which is confirmed by the IPF image (Fig. 26a). The influence of reinforced HEA particles, the hindering effect of HEA particles, and the ultrarefined structure of HEA-processed samples are attributed to higher mechanical properties [56]. FSP with WC tool used to reinforce AlSiBeTiV HEA particles on SS410 exhibits an enhanced microhardness and tensile strength of 518 HV and 896 MPa which is 47% and 49.8% respectively higher than the processed base metal. A 0.65 μm refined structure exhibited on HEA-processed samples leads to improved microhardness according to the Hall–Petch relationship. The reinforced HEA particles appear on the dimples of fractured tensile samples attributed to enhanced tensile strength by superior interfacial bonding (Fig. 26b). The evenly distributed HEA particles over the base metal are also the reason for enhanced results as shown in Fig. 26c [65]. A reciprocating friction process is employed on SS316L steel with $Al_{0.1}CoCrFeNi$ HEA particles exhibiting increased hardness by 2.5 times over base metal. The FSPed samples with 388 rpm demonstrate more strengthening mechanisms through nano-grains and nano-twins structure by grain-twin boundaries over FSPed samples with 1800 rpm. In addition, the ultrarefined structure is obtained by FSPed samples through a twining mechanism and high-density dislocation at 388 rpm (Fig. 26d) [159].
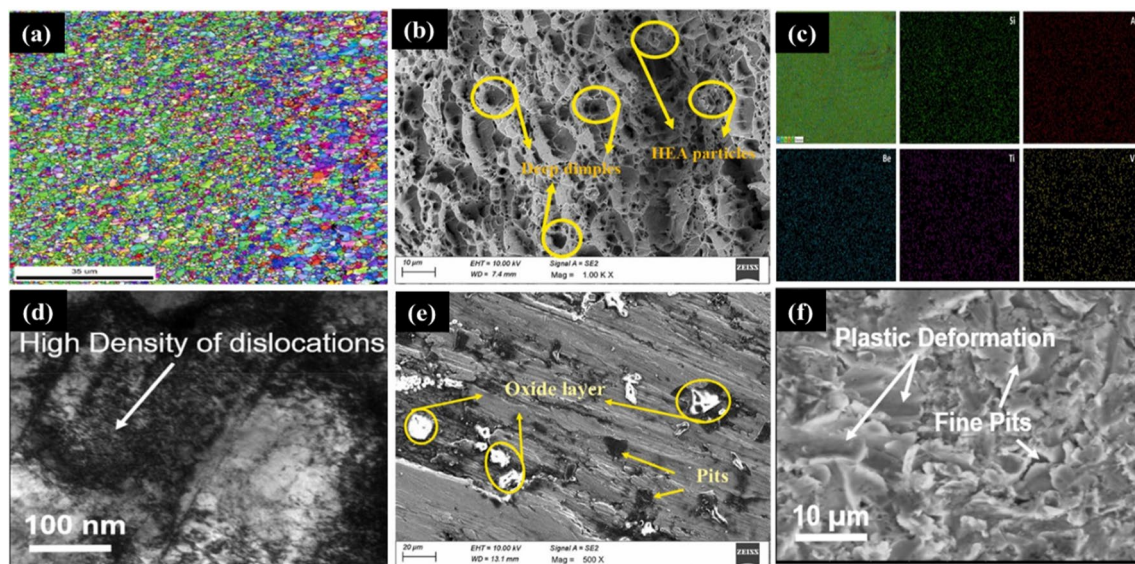
Fig. 26 **a** IPF image—refined grains distribution of FSPed CoCr-FeCuTi HEA/SS304L [56], **b** SEM image—HEA on dimples of FSPed AlSiBeTiV HEA/SS410 [65], **c** EDS elemental mapping of FSPed AlSiBeTiV HEA/SS410 [65], **d** SEM image—refined grains by high-density dislocation [159], **e** SEM image—oxide layer on worn surfaces [65], **f** SEM image—fine pits and grain size reduction [159]

7.2 Wear and Corrosion Behaviour of FSP on SS Alloys with HEA

The wear and corrosion behaviour of the FSPed SS base metal is improved by the reinforcement of HEA particles. The higher Hall–Petch relationship leads to enhanced wear resistance by refined grains, barrier effect, and the effective metallurgical bonding strength of HEA particles [65]. The formation of passivation films protect the sample surfaces against corrosion by the high entropy effect of HEA particles. The corrosion resistance improves by interfacial bonding and impediment of local anodic sites [193]. The FCC phase structure AlSiBeTiV HEA particles are reinforced on SS410 by FSP with a WC tapper cylindrical tool. The HEA-processed sample exhibits enhanced wear resistance by ultrarefined grains structure on pin-on-disc wear test. The grain growth is hindered by HEA particles, better interfacial bonding of HEA particles with base metal, and the formation of a protective layer on worn surfaces are attributed to improved wear resistance (Fig. 26e) [65]. The FSP with tapered WC tool used to reinforce CoCrFeCuTi HEA particles on SS304 exhibits a refined grain structure of 1.8 μm. The enhanced corrosion resistance is obtained under the 3.5 wt% NaCl electrolyte solution. The crack propagation is hindered by the influencing HEA particles, refined grain structure, and hindering effect of HEA particles [56]. $Al_{0.1}$CoCrFeNi HEA particles are reinforced with SS316L through a reciprocating friction process by a WC tool. The corrosion behaviour of the HEA-processed sample is analyzed with a 3.5 wt% NaCl electrolyte solution. The high corrosion resistance is obtained in the FSPed samples and the corrosion rate is reduced by 0.29 μA/cm^2. The deep craters and pits appear on the base metal and are minimized to very fine pits by grain size reduction through FSP as shown in Fig. 26f [159]. Table 7 presents the mechanical properties, wear and corrosion behaviour of base metal reinforced by HEA particles through FSP. The summarized data provides the research gap on SS base metal to enhance further research work.

8 Applications and Future Trends

The selection of multifunctional elements and synthesis methods of HEAs are essential for a specified application in the engineering industries. The as-cast HEA is used in both ambient and elevated temperatures in various fields such as rocket nozzle, nuclear construction, compressor and turbine blades of aero engines, transportation industries, and low-temperature applications like in the construction field, conducting materials as owned to its properties. It is possible to build nano-sized wire and rods using HEA particles and make their application as joining filler materials [139, 194, 195].

The as-cast HEA sample exhibits more hardness, higher wear, and corrosion resistance by fine grain structure and is evenly dispersed on the samples employed in structural machine components, tool, and die industry [20, 196]. The high corrosion resistance obtained on as-cast HEA is used in the marine industry, specifically in ship propellers by effective casting. The mechanical properties of AlCoCrFeNi HEA particles are increased at elevated temperatures through FSP. The higher heat resistance of HEA particles suits structural applications like aerospace engine components [197–199]. In structural applications, HEAs with Al matrix composites are effectively used owing to their combined effect of strength, ductility, thermo-mechanical stability, high specific stiffness, and fracture toughness [20, 200].

Due to the high ductile properties of HEA particles even at low temperatures, it could be used to produce micro instruments and small structured devices [201]. In magnetic devices, the eddy current losses are decreased by using a thin structured plate [202]. To increase the soft magnetic properties of HEA samples, the elements of Fe, Ni, and Co are incorporated into the HEA synthesis process. However, in the traditional fabrication process, it is difficult to achieve and apply it in high temperatures [197, 202]. The biocompatibility, wear, and corrosion resistance properties of titanium-based HEA reflect the same effect as natural bone in the area of biomedicine [203]. The high wear and corrosion resistance properties of Al_xCoCrFeNi HEA are used for the fabrication of medical instruments [204]. The HEA exhibits durability in electro-catalytic environments due

Table 7 Mechanical properties, wear, and corrosion behaviour of FSPed SS alloy samples

HEA particles	Hardness (HV)	YS* (MPa)	UTS (MPa)	EL* (%)	Wear resistance (%)	Corrosion rate (μA/cm^2)	Refs.
AlSiBeTiV	518	–	896	–	39.75%	–	[65]
CoCrFeCuTi	472	–	645	–	–	–	[56]
$Al_{0.1}$CoCrFeNi	530	–	–	–	–	0.29	[159]

YS yield strength, *EL* elongation

to their high corrosion and thermal resistance. Moreover, HEA particles lead an effective performance in methanol oxidation, water splitting, ammonia decomposition, and dye degradation [90]. The proper selection of FSP parameters, HEA elements, and synthesis methods with subsequent heat treatment and fabrication process environment is responsible for extensive application in the industries. The summarized applications are depicted in Fig. 27.

The reinforcement of novel HEA over metals is promised to improve the mechanical properties, wear, and corrosion resistance through a single-step FSP. Even though FSPed HEA/as cast specimens have great potential to serve in the current scenario, some of the challenges arising during FSP lead to limitations in the application. The challenges and the possible future scopes are discussed subsequently.

- The residual stress, segregation of elements, and dendritic structure are obtained in the synthesis of HEA due to the melting temperature difference of principal elements. To overcome this, more attention has been required on the subsequent processes such as heat treatment and cooling rate.
- In solid-state synthesis, mechanical alloying is employed to obtain a single phase solid-structure by varying milling time. The other milling parameters as milling speed, the atmosphere of milling, and milling media could be taken into account in the future for obtaining optimal homogenous phase by mechanical alloying.
- Major studies gone through FSP/HEA with similar metals and influences of FSP parameters are discussed so far. However, studies conducted on dissimilar metals with HEA particles reinforced by FSP and their effects on microstructure and properties are still to be explored.
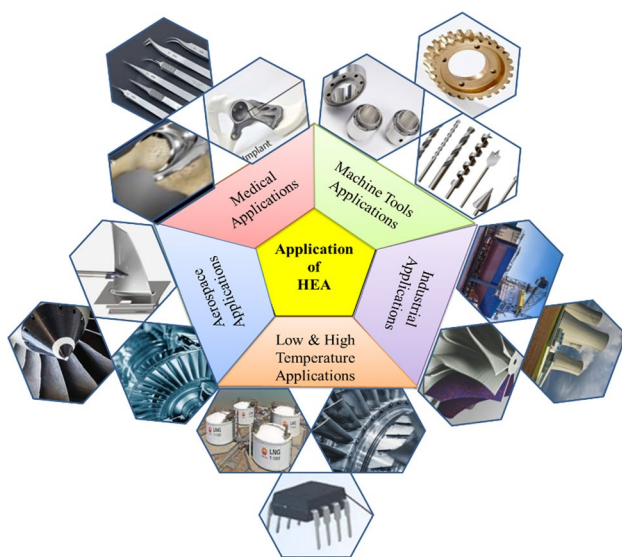

Fig. 27 Applications of the HEAs processed by FSP

- The microstructure, nature of phase, the progression of mechanical properties, wear and corrosion resistance, fatigue behaviour, and thermo-mechanical stability of FSPed HEA samples could not be predicted before experimentation. Because several dependent factors such as the nature of principal elements, melting temperature of elements used in HEA, mode of synthesis, the subsequent process employed, ambient condition, and FSP parameters are considered for the improvement of processed samples.
- In recent studies, FSP is employed on the plain surface of the as-cast metal. However, in real-time applications, complex shape structures are employed. Therefore, the influences of FSP on complex structures and their metal properties is a challenging process and needs to be studied in the future.
- The more expensive tools (W–Re, PCBN) are used for hard and high melting temperature materials including titanium, steel, and ceramic particle-based composites. Moreover, the tools exhibit relatively less fracture toughness leading to the limitation in usage. Hence, a long-lasting and economical tool for hard materials has to be further explored.
- Significant studies are available in alloy and metal-based composites processed by FSP. Research on low melting temperature materials such as polymer-based composite materials, and other non-metallic materials could be of interest.
- High-performance features are obtained on FSPed samples by refined grains with unique phase structures by optimizing the process parameter variables. Moreover, the cooling system and environmental nature of FSP is also a factor for optimal grain size reduction. Hence, it can be a focus on interest.
- Numerous studies are available on various materials processed by FSP at the laboratory level. Consequently, a great many attempts are required on FSP to the transformation from research-based work to industry-responsive processes.

9 Conclusions

The review article provides a comprehensive analysis of the current state of research in FSP using HEAs. The use of HEAs in FSP has demonstrated several advantages, such as improved mechanical properties, enhanced wear resistance, and increased thermal stability, compared to traditional alloys. This article highlights the various parameters involved in FSP, different HEAs and their impact on the microstructure and mechanical properties of the processed material. Additionally, the challenges associated with FSP using HEAs are reviewed. The research gap associated

with the FSP process and its extension over various materials is also discussed. The possible applications are also reviewed based on their properties. Overall, this review concludes that FSP using HEAs has the potential to revolutionize the manufacturing of advanced materials, particularly in the aerospace and automotive industries.

Declarations

Conflict of interests The authors declare that they have no known competing financial interests or personal relationships that could have appeared to influence the work reported in this paper.

References

1. E.P. George, D. Raabe, R.O. Ritchie, Nat. Rev. Mater. **4**, 515 (2019)
2. J.E. Gray, B. Luan, J. Alloys Compd. **336**, 88 (2002)
3. Y. Qin, Y. Wang, S. Guan, C. Wang, B. Jiang, W. Wang, M. Huang, B. Peng, Q. Li, F. Peng, Z. Kou, Int. J. Refract. Met. Hard Mater. **102**, 105718 (2022)
4. N. Radhika, M. Sam, M. Sathishkumar, V. Kavimani, A. Pramanik, Adv. Mater. Process. Technol. (2023). https://doi.org/10.1080/2374068X20232216397
5. A. Jamwal, P. Mittal, R. Agrawal, S. Gupta, D. Kumar, K.K. Sadasivuni, P. Gupta, J. Compos. **54**, 2635 (2020)
6. T. He, O. Ertuğrul, N. Ciftci, V. Uhlenwinkel, K. Nielsch, S. Scudino, Mater. Sci. Eng. A **742**, 517 (2019)
7. Z.Y. Liu, S.J. Xu, B.L. Xiao, P. Xue, W.G. Wang, Z.Y. Ma, Compos. Part A Appl. Sci. Manuf. **43**, 2161 (2012)
8. Y. Wang, Y. Chen, J. Xie, J. Ni, T. Zhang, S. Wang, L. Yin, Mater. Sci. Eng. A **854**, 143789 (2022)
9. T.W. Lu, W.P. Chen, P. Wang, M.D. Mao, Y.X. Liu, Z.Q. Fu, J. Alloys Compd. **735**, 1137 (2018)
10. Z.G. Xu, L.T. Jiang, Q. Zhang, J. Qiao, D. Gong, G.H. Wu, Mater. Des. **111**, 375 (2016)
11. J. Li, Y. Li, F. Wang, X. Meng, L. Wan, Z. Dong, Y. Huang, Mater. Sci. Eng. A **792**, 139755 (2020)
12. R. Jojith, N. Radhika, Part. Sci. Technol. **37**, 566 (2018)
13. N. Radhika, T. Balaji, S. Palaniappan, J. Eng. Sci. Technol. **10**, 134 (2015)
14. S. Liu, Y. Wang, T. Muthuramalingam, G. Anbuchezhiyan, Compos. B Eng. **176**, 107329 (2019)
15. R. Prabakaran, A. Sait, V. Senthilkumar, Mech. Mech. Eng. **21**, 415 (2017)
16. W.J. Cantwell, J. Morton, J. Strain Anal. Eng. Des. **27**, 29 (1992)
17. J.W. Yeh, S.K. Chen, S.J. Lin, J.Y. Gan, T.S. Chin, T.T. Shun, C.H. Tsau, S.Y. Chang, Adv. Eng. Mater. **6**, 299 (2004)
18. A.J. Zaddach, C. Niu, A.A. Oni, M. Fan, J.M. LeBeau, D.L. Irving, C.C. Koch, Intermetallics **68**, 107 (2016)
19. Y. Zhou, Y. Zhang, X. Wang, Y. Wang, G. Chen, Rare Met. **27**, 627 (2008)
20. Y. Zhang, T.T. Zuo, Z. Tang, M.C. Gao, K.A. Dahmen, P.K. Liaw, Z.P. Lu, Prog. Mater. Sci. **61**, 1 (2014)
21. M.C. Gao, P.K. Liaw, J.W. Yeh, Y. Zhang, *High-Entropy Alloys: Fundamentals and Applications* (Springer, Cham, 2016), pp.1–516
22. J. Sure, D.S.M. Vishnu, C. Schwandt, Appl. Mater. Today **9**, 111 (2017)
23. R. Feng, M.C. Gao, C. Zhang, W. Guo, J.D. Poplawsky, F. Zhang, J.A. Hawk, J.C. Neuefeind, Y. Ren, P.K. Liaw, Acta Mater. **146**, 280 (2018)
24. K.K. Tseng, Y.C. Yang, C.C. Juan, T.S. Chin, C.W. Tsai, J.W. Yeh, Sci. China Technol. Sci. **61**, 184 (2018)
25. M.G. Poletti, C.M. McCaughey, G. Fiore, R. Goodall, L. Battezzati, Int. J. Refract. Met. Hard Mater. **76**, 128 (2018)
26. W. Xiong, A.X.Y. Guo, S. Zhan, C.T. Liu, S.C. Cao, J. Mater. Sci. Technol. **142**, 196 (2023)
27. D. Wu, K. Kusada, T. Yamamoto, T. Toriyama, S. Matsumura, S. Kawaguchi, Y. Kubota, H. Kitagawa, J. Am. Chem. Soc. **142**, 13833 (2020)
28. D. Wu, K. Kusada, T. Yamamoto, T. Toriyama, S. Matsumura, I. Gueye, O. Seo, J. Kim, S. Hiroi, O. Sakata, S. Kawaguchi, Y. Kubota, H. Kitagawa, Chem. Sci. **11**, 12731 (2020)
29. D.B. Miracle, O.N. Senkov, Acta Mater. **122**, 448 (2017)
30. J. Yi, S. Tang, M. Xu, L. Yang, L. Wang, L. Zeng, J. Alloys Compd. **846**, 156466 (2020)
31. W. Kucza, J. Alloys Compd. **894**, 162443 (2022)
32. I. Opahle, H.K. Singh, J. Zemen, O. Gutfleisch, H. Zhang, Phys. Rev. Res. **2**, 023134 (2020)
33. K.J. Laws, C. Crosby, A. Sridhar, P. Conway, L.S. Koloadin, M. Zhao, S. Aron-Dine, L.C. Bassman, J. Alloys Compd. **650**, 949 (2015)
34. J. Chen, X. Zhou, W. Wang, B. Liu, Y. Lv, W. Yang, D. Xu, Y. Liu, J. Alloys Compd. **760**, 15 (2018)
35. P. Sharma, V.K. Dwivedi, S.P. Dwivedi, Mater. Today Proc. **43**, 502 (2021)
36. S.A.E. Mobarakeh, K. Dehghani, J. Mater. Res. Technol. **19**, 765 (2022)
37. R. Bauri, D. Yadav, G. Suhas, Mater. Sci. Eng. A **528**, 4732 (2011)
38. G.K. Padhy, C.S. Wu, S. Gao, J. Mater. Sci. Technol. **34**, 1 (2018)
39. Z.Y. Ma, S.R. Sharma, R.S. Mishra, Mater. Sci. Eng. A **433**, 269 (2006)
40. X. Yang, Z. Yan, P. Dong, B. Cheng, J. Zhang, T. Zhang, H. Zhang, W. Wang, Surf. Coat. Technol. **385**, 125438 (2020)
41. R.S. Mishra, Z.Y. Ma, Mater. Sci. Eng. R. Rep. **50**, 1 (2005)
42. Z.Y. Ma, Metall. Mater. Trans. A Phys. Metall. Mater. Sci. **39**, 642 (2008)
43. M.S. Węglowski, Arch. Civ. Mech. Eng. **18**, 114 (2018)
44. G.R. Argade, K. Kandasamy, S.K. Panigrahi, R.S. Mishra, Corros. Sci. **58**, 321 (2012)
45. V. Sharma, U. Prakash, B.V.M. Kumar, J. Mater. Process. Technol. **224**, 117 (2015)
46. V.R. Malik, P.A. Bajakke, K.K. Saxena, A. Lakshmikanthan, A.S. Deshpande, S. Mabuwa, V. Masomi, Mater. Res. Express **9**, 066507 (2022)
47. E.R.I. Mahmoud, H. Almohamadi, A. Aljabri, S.Z. Khan, A.N. Saquib, M. Farhan, M.A.G. Elkotb, Materials **14**, 7611 (2021)
48. B.R. Sunil, G.P.K. Reddy, H. Patle, R. Dumpala, J. Magne. Alloys **4**, 52 (2016)
49. S. Rathee, S. Maheshwari, A.N. Siddiquee, M. Srivastava, Crit. Rev. Solid State Mater. Sci. **43**, 334 (2018)
50. E.A. El-Danaf, M.M. El-Rayes, M.S. Soliman, Mater. Des. **31**, 1231 (2010)
51. J. Chen, X. Jiang, H. Sun, Z. Shao, Y. Fang, R. Shu, Nanotechnol. Rev. **10**, 1116 (2021)
52. Z. Zhang, D.L. Chen, Mater. Sci. Eng. A **483–484**, 148 (2008)
53. H. Zhang, K. Ma, B. Zhang, J. Song, Q. Gao, L. Yu, J. Mater. Sci. **57**, 20002 (2022)
54. N. Kumar, M. Komarasamy, P. Nelaturu, Z. Tang, P.K. Liaw, R.S. Mishra, J. Mater. Sci. **67**, 1007 (2015)
55. S.Y. Anaman, S. Ansah, H.H. Cho, M.G. Jo, J.Y. Suh, M. Kang, J.S. Lee, S.T. Hong, H.N. Han, J. Mater. Sci. Technol. **87**, 60 (2021)

56. S.A. Krishna, N. Radhika, B. Saleh, S. Manivannan, J. Alloys Compd. **953**, 170153 (2023)

57. H. Moghanni, K. Dehghani, A. Shafiei, J. Mater. Res. Technol. **16**, 1069 (2022)

58. S.P. Ju, I.J. Lee, H.Y. Chen, J. Alloys Compd. **858**, 157681 (2021)

59. Z. Fu, W. Chen, H. Wen, D. Zhang, Z. Chen, B. Zheng, Y. Zhou, E.J. Lavernia, Acta Mater. **107**, 59 (2016)

60. T. Yang, S. Xia, S. Liu, C. Wang, S. Liu, Y. Zhang, J. Xue, S. Yan, Y. Wang, Mater. Sci. Eng. A **648**, 15 (2015)

61. R. Chen, G. Qin, H. Zheng, L. Wang, Y. Su, Y.L. Chiu, H. Ding, J. Guo, H. Fu, Acta Mater. **144**, 129 (2018)

62. K.K. Alaneme, M.O. Bodunrin, S.R. Oke, J. Mater. Res. Technol. **5**, 384 (2016)

63. S. Syed Ghazi, K.R. Ravi, Intermetallics (Barking) **73**, 40 (2016)

64. Y.A. Alshataif, S. Sivasankaran, F.A. Al-Mufadi, A.S. Alaboodi, H.R. Ammar, Met. Mater. Int. **26**, 1099 (2020)

65. S. Ragunath, N. Radhika, S. Aravind Krishna, N. Jeyaprakash, Tribol. Int. **188**, 108840 (2023)

66. X. Yang, P. Dong, Z. Yan, B. Cheng, X. Zhai, H. Chen, H. Zhang, W. Wang, J. Alloys Compd. **836**, 155411 (2020)

67. M. Vaidya, G.M. Muralikrishna, B.S. Murty, J. Mater. Res. **34**, 664 (2019)

68. I. Moravcik, J. Cizek, P. Gavendova, S. Sheikh, S. Guo, I. Dlouhy, Mater. Lett. **174**, 53 (2016)

69. Ł Rogal, D. Kalita, A. Tarasek, P. Bobrowski, F. Czerwinski, J. Alloys Compd. **708**, 344 (2017)

70. Z. Fu, W. Chen, Z. Jiang, B.E. MacDonald, Y. Lin, F. Chen, L. Zhang, E.J. Lavernia, Powder Metall. **61**, 106 (2018)

71. X.R. Tan, G.P. Zhang, Q. Zhi, Z.X. Liu, Mater. Des. **109**, 27 (2016)

72. C. Suryanarayana, Prog. Mater. Sci. **46**, 1 (2001)

73. S. Rajendrachari, V. Adimule, M. Gulen, F. Khosravi, K.K. Somashekharappa, Materials. **15**, 7591 (2022)

74. L. Sang, Y. Xu, J. Non Cryst. Solids **530**, 119854 (2020)

75. R.K. Prabakaran, A.N. Sait, V. Senthilkumar, Mech. Mech. Eng. **21**, 823 (2017)

76. M.D. Alcala, C. Real, I. Fombella, I. Trigo, J.M. Cordoba, J. Alloys Compd. **749**, 834 (2018)

77. S. Varalakshmi, M. Kamaraj, B.S. Murty, J. Alloys Compd. **460**, 253 (2008)

78. P. Wang, H. Cai, S. Zhou, L. Xu, J. Alloys Compd. **695**, 462 (2017)

79. C. Wang, W. Ji, Z. Fu, Adv. Powder Technol. **25**, 1334 (2014)

80. T. Lu, S. Scudino, W. Chen, P. Wang, D. Li, M. Mao, L. Kang, Y. Liu, Z. Fu, Mater. Sci. Eng. A **726**, 126 (2018)

81. W. Ji, W. Wang, H. Wang, J. Zhang, Y. Wang, F. Zhang, Z. Fu, Intermetallics **56**, 24 (2015)

82. M.R. Toroghinejad, H. Pirmoradian, A. Shabani, Mater. Chem. Phys. **289**, 126433 (2022)

83. J. Dunkley Dr, *Advances in Powder Metallurgy: Properties, Processing and Applications* (Elsevier, Amsterdam, 2013), p.3

84. C.C. Yang, J.L. Hang Chau, C.J. Weng, C.S. Chen, Y.H. Chou, Mater. Chem. Phys. **202**, 151 (2017)

85. I. Kunce, M. Polanski, K. Karczewski, T. Plocinski, K.J. Kurzydlowski, J. Alloys Compd. **648**, 751 (2015)

86. Y. Liu, J. Wang, Q. Fang, B. Liu, Y. Wu, S. Chen, Intermetallics **68**, 16 (2016)

87. Z. Ren, S. Zhu, X. Wang, Y. Zhao, G. Han, K. Zhou, W. Wang, G. Tian, Metals **13**, 432 (2023)

88. S.M. Chiu, T.T. Lin, R.K. Sammy, N.G. Kipkirui, Y.Q. Lin, J.T. Liang, S.H. Chen, Mater. Chem. Phys. **275**, 125194 (2022)

89. J. Lu, L. Li, H. Zhang, Y. Chen, L. Luo, X. Zhao, F. Guo, P. Xiao, Corros. Sci. **181**, 109257 (2021)

90. L.H. Liu, N. Li, M. Han, J.R. Han, H.Y. Liang, Rare Metels. **41**, 125 (2022)

91. A. Arab, Y. Guo, Q. Zhou, P. Chen, Entropy **21**, 880 (2019)

92. L.E. Geambazu, C.M. Cotruţ, F. Miculescu, I. Csaki, Mater. **14**, 3802 (2021)

93. Y. Long, K. Su, J. Zhang, X. Liang, H. Peng, X. Li, Materials **11**, 669 (2018)

94. Y. Sun, B. Ke, Y. Li, K. Yang, M. Yang, W. Ji, Z. Fu, Entropy **21**, 122 (2019)

95. S. Varalakshmi, M. Kamaraj, B.S. Murty, Mater. Sci. Eng. A **527**, 1027 (2010)

96. L. Moravcikova-Gouvea, I. Moravcik, V. Pouchly, Z. Kovacova, M. Kitzmantel, E. Neubauer, I. Dlouhy, Materials **14**, 5796 (2021)

97. L. Moravcikova-Gouvea, I. Moravcik, M. Omasta, J. Veselý, J. Cizek, P. Minárik, J. Cupera, A. Záděra, V. Jan, I. Dlouhy, Mater Charact **159**, 110046 (2020)

98. S.P. Wang, J. Xu, Mater. Sci. Eng. C **73**, 80 (2017)

99. N. Noble, N. Radhika, M. Sathishkumar, B. Saleh, Tribol. Int. **185**, 108525 (2023)

100. X. Yang, H. Zhang, P. Dong, Z. Yan, W. Wang, Mater Charact **183**, 111646 (2022)

101. P. Han, W. Wang, Z. Liu, T. Zhang, Q. Liu, X. Guan, K. Qiao, D. Ye, Y. Cai, Y. Xie, K. Wang, J. Alloys Compd. **907**, 164426 (2022)

102. L.H. Wu, X.B. Hu, X.X. Zhang, Y.Z. Li, Z.Y. Ma, X.L. Ma, B.L. Xiao, Acta Mater. **166**, 371 (2019)

103. R.S. Mishra, M.W. Mahoney, S.X. McFadden, N.A. Mara, A.K. Mukherjee, Scr. Mater. **42**, 163 (1999)

104. B. Wu, M.Z. Ibrahim, S. Raja, F. Yusof, B.B. Abdul Razak, M.R. Bin Muhamad, R. Huang, Y. Zhang, I.A. Badruddin, M. Hussien, S. Kamangar, J. Mater. Res. Technol. **20**, 1940 (2022)

105. A. Sharma, Coatings **11**, 372 (2021)

106. M. Sathish, N. Radhika, B. Saleh, Met. Mater. Int. **29**, 1229 (2022)

107. A.M. Ralls, A.K. Kasar, P.L. Menezes, J. Manuf. Mater. Process. **5**, 97 (2021)

108. N. Merah, M.A. Azeem, H.M. Abubaker, F. Al-Badour, J. Albinmousa, A.A. Sorour, Materials **14**, 5023 (2021)

109. Z. Nasiri, M. SarkariKhorrami, H. Mirzadeh, M. Emamy, Mater. Lett. **296**, 129880 (2021)

110. Y. Mazaheri, M.M. Jalilvand, A. Heidarpour, A.R. Jahani, Tribol. Int. **143**, 106062 (2020)

111. H. Mirzadeh, Mater. Sci. Eng. A **819**, 145403 (2021)

112. A.P. Zykova, S.Y. Tarasov, A.V. Chumaevskiy, E.A. Kolubaev, Metals (Basel) **10**, 1 (2020)

113. S.R. Sharma, Z.Y. Ma, R.S. Mishra, Scr. Mater. **51**, 237 (2004)

114. T. Wang, M. Komarasamy, S. Shukla, R.S. Mishra, J. Alloys Compd. **766**, 312 (2018)

115. F. Xiong, R. Dong Fu, Y. Jun Li, D. Li Sang, J. Alloys Compd. **822**, 153512 (2020)

116. J.W. Simmons, Mater. Sci. Eng. A **207**, 159 (1996)

117. G. Huang, J. Wu, W. Hou, Y. Shen, Mater. Sci. Eng. A **734**, 353 (2018)

118. X. Feng, H. Liu, J.C. Lippold, Mater Charact **82**, 97 (2013)

119. S. Bharti, N.D. Ghetiya, K.M. Patel, Mater. Manuf. Process. **36**, 135 (2021)

120. L. Dutta, B. Thakur, Singh. Mater. Res. Express **9**, 096516 (2022)

121. S. Aliakbari, M. Ketabchi, S.E. Mirsalehi, J. Manuf. Process. **35**, 226 (2018)

122. L. Karthikeyan, V.S. Senthilkumar, K.A. Padmanabhan, Mater. Des. **31**, 761 (2010)

123. A. Kurt, I. Uygur, E. Cete, J. Mater. Process. Technol. **211**, 313 (2011)

124. Y. Morisada, H. Fujii, T. Nagaoka, K. Nogi, M. Fukusumi, Compos. Part A Appl. Sci. Manuf. **38**, 2097 (2007)

125. R. Bauri, Bull. Mater. Sci. **37**, 571 (2014)

126. M. Azizieh, A.H. Kokabi, P. Abachi, Mater. Des. **32**, 2034 (2011)

127. D. Khayyamin, A. Mostafapour, R. Keshmiri, Mater. Sci. Eng. A **559**, 217 (2013)

128. A. Dolatkhah, P. Golbabaei, M.K. Besharati Givi, F. Molaiekiya, Mater. Des. **37**, 458 (2012)

129. X. Feng, H. Liu, S. Suresh Babu, Scr. Mater. **65**, 1057 (2011)

130. F. Eskandari, M. Atapour, M.A. Golozar, B. Sadeghi, P. Cavaliere, Tribol. Mater. Surf. Interfaces **13**, 172 (2019)

131. S. Ghadar, A. Momeni, E. Khademi, S. Kazemi, Mater. Sci. Eng. B **263**, 114813 (2021)

132. P. Sagar, A. Handa, Mater. Today. Proc. **38**, 198 (2021)

133. B. Bagheri, A. Abdollahzadeh, F. Sharifi, M. Abbasi, Proc. Inst. Mech. Eng. C J. Mech. Eng. Sci. **236**, 2312 (2022)

134. F. Yousefpour, R. Jamaati, H. Jamshidi Aval, J. Mech. Behav. Biomed. Mater. **125**, 104894 (2022)

135. M. Paidar, O.O. Ojo, H.R. Ezatpour, A. Heidarzadeh, Surf. Coat. Technol. **361**, 159 (2019)

136. M. Vakili-Azghandi, M. Roknian, J.A. Szpunar, S.M. Mousavizade, J. Alloys Compd. **816**, 152557 (2020)

137. M.M. El-Rayes, E.A. El-Danaf, J. Mater. Process. Technol. **212**, 1157 (2012)

138. Z.Y. Ma, S.R. Sharma, R.S. Mishra, Scr. Mater. **54**, 1623 (2006)

139. A. Mishra, Weld. Tech. Rev. **93**, 27 (2021)

140. J. Zhang, R. Fu, Y. Li, L. Lei, L. Guo, H. Lv, J. Yang, J. Alloys Compd. **927**, 167015 (2022)

141. H. Mehdi, R.S. Mishra, Adv. Ind. Manuf. Eng. **3**, 100062 (2021)

142. G. Girish, V. Anandakrishnan, J. Mater. Eng. Perform. **30**, 5868 (2021)

143. M. Barmouz, M.K.B. Givi, J. Jafari, J. Mater. Eng. Perform. **23**, 101 (2014)

144. L. Karthikeyan, V.S. Senthil Kumar, Mater. Des. **32**, 3085 (2011)

145. S. Rathee, S. Maheshwari, A. Noor Siddiquee, M. Srivastava, S. Kumar Sharma, Mater. Today Proc. **3**, 4151 (2016)

146. A. Shamsipur, S.F. Kashani-Bozorg, A. Zarei-Hanzaki, Surf. Coat. Technol. **206**, 1372 (2011)

147. S. Bhowmik, J. Zhang, S.C. Vogel, S.S. Nene, R.S. Mishra, B.A. McWilliams, M. Knezevic, J. Alloys Compd. **891**, 161871 (2022)

148. S.S. Nene, M. Frank, K. Liu, S. Sinha, R.S. Mishra, B. McWilliams, K.C. Cho, Scr. Mater. **154**, 163 (2018)

149. V.V. Patel, V. Badheka, A. Kumar, J. Mater. Process. Technol. **240**, 68 (2017)

150. A. Thakur, S.M. Akram, S.K.M. Waseem, S. Kanojiya, L.R. Gupta, R. Wandra, Mater. Today Proc. **50**, 684 (2022)

151. K.W. Liew, Y.Z. Chung, G.S. Teo, C.K. Kok, Metals **11**, 1695 (2021)

152. L. Tonelli, A. Morri, S. Toschi, M. Shaaban, H.R. Ammar, M.M.Z. Ahmed, R.M. Ramadan, I. El-Mahallawi, L. Ceschini, Int. J. of Adv. Manuf. Technol. **102**, 3945 (2019)

153. J. John, S.P. Shanmughanatan, M.B. Kiran, Mater. Today Proc. **5**, 2965 (2018)

154. R. Bauri, G.D. Janaki Ram, D. Yadav, C.N. Shyam Kumar, Mater. Today Proc. **2**, 3203 (2015)

155. V.M. Khojastehnezhad, H.H. Pourasl, R. VatankhahBarenji, Proc. Inst. Mech. Eng. Pt. L J. Mater. Des. Appl. **233**, 900 (2017)

156. N. Gangil, S. Maheshwari, A. N. Siddiquee, Mech. Ind. **19** (2018).

157. S. Rathee, S. Maheshwari, A.N. Siddiquee, M. Srivastava, Def. Technol. **13**, 86 (2017)

158. A. Adetunla, E. Akinlabi, Mater. Res. Express **5**, 115015 (2018)

159. H.S. Arora, S. Pradhan, A. Kumar, G. Perumal, R. Salloom, S. Mukherjee, H.S. Grewal, Wear **456–457**, 203385 (2020)

160. K. Liu, S.S. Nene, M. Frank, S. Sinha, R.S. Mishra, Appl. Mater. Today **15**, 525 (2019)

161. S. Sinha, S.S. Nene, M. Frank, K. Liu, R.A. Lebensohn, R.S. Mishra, Acta Mater. **184**, 164 (2020)

162. C.J. Lee, J.C. Huang, P.L. Hsieh, Key Eng. Mater. **313**, 69 (2006)

163. D. Ahmadkhaniha, M. Heydarzadeh Sohi, A. Zarei-Hanzaki, S.M. Bayazid, M. Saba, J. Magne, Alloys **3**, 168 (2015)

164. K.H. Raj, R.S. Sharma, P. Singh, A. Dayal, Procedia Eng. **10**, 2904 (2011)

165. C. Chanakyan, S. Sivasankar, M. Meignanamoorthy, M. Ravichandran, V. Mohanavel, S. Alfarraj, H.S. Almoallim, V. Manikandan, J. Isaac Joshuaramesh Lalvani, Adv. Mater. Sci. Eng. **2021**, 6450251 (2021)

166. M. Puviyarasan, V.S. Senthil Kumar, Procedia Eng. **38**, 1094 (2012)

167. M. Regev, S. Spigarelli, C. Cervera, C. Garcia-Mateo, Metals **11**, 656 (2021)

168. R. Butola, M.S. Ranganath, Q. Murtaza, Eng. Res. Express **1**, 025015 (2019)

169. S. Sinha, S.S. Nene, M. Frank, K. Liu, R.S. Mishra, B.A. McWilliams, K.C. Cho, Materialia **6**, 100310 (2019)

170. S. Seenivasan, K. Soorya Prakash, S. Nandhakumar, P.M. Gopal, Proc. Inst. Mech. Eng. C J. Mech. Eng. Sci. **235**, 5555 (2021)

171. N. Li, C.L. Jia, Z.W. Wang, L.H. Wu, D.R. Ni, Z.K. Li, H.M. Fu, P. Xue, B.L. Xiao, Z.Y. Ma, Y. Shao, Y.L. Chang, Acta Metall. Sini. **33**, 947 (2020)

172. R.B. Nair, H.S. Arora, H.S. Grewal, Int. J. Miner. Metall. Mater. **27**, 1353 (2020)

173. T. Wang, S. Shukla, M. Komarasamy, K. Liu, R.S. Mishra, Mater. Lett. **236**, 472 (2019)

174. N. Meena, A.G. Rao, S.G. Dommeti, N. Prabhu, Lubricants **11**, 2 (2022)

175. S.A.E. Mobarakeh, T. Seyedhosseini, K. Dehghani, J. Alloys Compd. **896**, 163052 (2022)

176. S. Shukla, T. Wang, M. Frank, P. Agrawal, S. Sinha, R.A. Mirshams, R.S. Mishra, Mater. Today Commun. **23**, 100869 (2020)

177. C. Zhang, K. Feng, H. Kokawa, Z. Li, K. Chen, Mater. Sci. Eng. A **845**, 143254 (2022)

178. A. Sittiho, M. Bhattacharyya, J. Graves, S.S. Nene, R.S. Mishra, I. Charit, Mater. Today Commun. **28**, 102635 (2021)

179. V. Patel, W. Li, A. Vairis, V. Badheka, Crit. Rev. Solid State Mater. Sci. **44**, 378 (2019)

180. T. Satish Kumar, S. Shalini, G. Suganya Priyadharshini, R. Subramanian, Int. J. Mater. Res. **110**, 114 (2019)

181. T. Satish Kumar, G. Suganya Priyadharshini, S. Shalini, K. Krishna Kumar, R. Subramanian, Trans. Indian Inst. Met. **72**, 1593 (2019)

182. J. Gao, X. Wang, S. Zhang, L. Yu, J. Zhang, Y. Shen, Int. J. Adv. Manuf. Technol. **110**, 569 (2020)

183. H. Jie Zhang, Z. Jie Ji, H. Jie Liu, H. Zhang, S. Hua Luo, R. Bin Mei, Y. Ling Wang, J. Mater. Eng. Perform. **29**, 4206 (2020)

184. X. Yang, H. Zhang, B. Cheng, Y. Liu, Z. Yan, P. Dong, W. Wang, Surf. Topogr. **8**, 035012 (2020)

185. P. Han, J. Lin, W. Wang, Z. Liu, Y. Xiang, T. Zhang, Q. Liu, X. Guan, K. Qiao, Y. Xie, K. Wang, Met. Mater. Int. **29**, 845 (2022)

186. X. Yang, X. Zhai, P. Dong, Z. Yan, B. Cheng, H. Zhang, W. Wang, Mater. Lett. **275**, 128200 (2020)

187. H.S. Kim, Mater. Sci. Eng. A **289**, 30 (2000)

188. M. Barmouz, P. Asadi, M.K. Besharati Givi, M. Taherishargh, Mater. Sci. Eng. A **528**, 1740 (2011)

189. R. Zhu, R. Li, Y. Sun, J. Feng, W. Gong, J. Alloys Compd. **940**, 168906 (2023)

190. P. Asadi, G. Faraji, A. Masoumi, M.K.B. Givi, Metall. Mater. Trans. A Phys. Metall. Mater. Sci. **42**, 2820 (2011)

191. K.D. Ralston, N. Birbilis, C.H.J. Davies, Scr. Mater. **63**, 1201 (2010)

192. Z.F. He, N. Jia, D. Ma, H.L. Yan, Z.M. Li, D. Raabe, Mater. Sci. Eng. A **759**, 437 (2019)

193. Y. Fu, J. Li, H. Luo, C. Du, X. Li, J. Mater. Sci. Technol. **80**, 217 (2021)

194. V. Geanta, I. Voiculescu, *Engineering Steels and High Entropy-Alloys* (IntechOpen, London, 2019)
195. A. Sharma, *Engineering Steels and High Entropy-Alloys* (IntechOpen, London, 2020), p.223
196. D.B. Miracle, J.D. Miller, O.N. Senkov, C. Woodward, M.D. Uchic, J. Tiley, Entropy **16**, 494 (2014)
197. M. Tokarewicz, M. Grądzka-Dahlke, Metals (Basel) **11**, 1302 (2021)
198. K.R. Lim, K.S. Lee, J.S. Lee, J.Y. Kim, H.J. Chang, Y.S. Na, J. Alloys Compd. **728**, 1235 (2017)
199. J.W. Yeh, S.J. Lin, J. Mater. Res. **33**, 3129 (2018)
200. D. Choudhuri, M. Komarasamy, V. Ageh, R.S. Mishra, Mater. Chem. Phys. **217**, 308 (2018)
201. W.B. Liao, H. Zhang, Z.Y. Liu, P.F. Li, J.J. Huang, C.Y. Yu, Y. Lu, Entropy **21**, 146 (2019)
202. X. Yan, Y. Zhang, Scr. Mater. **187**, 188 (2020)
203. N. Ma, S. Liu, W. Liu, L. Xie, D. Wei, L. Wang, L. Li, B. Zhao, Y. Wang, Front. Bioeng. Biotechnol. **8**, 603522 (2020)
204. P.P. Socorro-Perdomo, N.R. Florido-Suárez, I. Voiculescu, J.C. Mirza-Rosca, Metals **11**, 928 (2021)